

ARTICLE

A mitochondrial contribution to anti-inflammatory shear stress signaling in vascular endothelial cells

Brian G. Coon¹, Sushma Timalsina¹, Matteo Astone², Zhen W. Zhuang¹, Jennifer Fang¹, Jinah Han¹, Jurgen Themen¹, Minhwan Chung¹, Young Joo Yang-Klingler³, Mukesh Jain⁴, Karen K. Hirschi¹, Ai Yamamoto³, Louis-Eric Trudeau⁵, Massimo Santoro², and Martin A. Schwartz^{1,6,7}

Atherosclerosis, the major cause of myocardial infarction and stroke, results from converging inflammatory, metabolic, and biomechanical factors. Arterial lesions form at sites of low and disturbed blood flow but are suppressed by high laminar shear stress (LSS) mainly via transcriptional induction of the anti-inflammatory transcription factor, Kruppel-like factor 2 (*Klf2*). We therefore performed a whole genome CRISPR-Cas9 screen to identify genes required for LSS induction of *Klf2*. Subsequent mechanistic investigation revealed that LSS induces *Klf2* via activation of both a MEKK2/3–MEK5–ERK5 kinase module and mitochondrial metabolism. Mitochondrial calcium and ROS signaling regulate assembly of a mitophagy- and p62-dependent scaffolding complex that amplifies MEKK–MEK5–ERK5 signaling. Blocking the mitochondrial pathway in vivo reduces expression of *KLF2*-dependent genes such as eNOS and inhibits vascular remodeling. Failure to activate the mitochondrial pathway limits *Klf2* expression in regions of disturbed flow. This work thus defines a connection between metabolism and vascular inflammation that provides a new framework for understanding and developing treatments for vascular disease.

Introduction

Laminar shear stress (LSS) from blood flow, acting on vascular endothelial cells (ECs), stabilizes blood vessels and protects against disease (Jain et al., 2014). The transcription factor Kruppel-like factor 2 (KLF2) is the principal mediator of this protective effect (Nakamura and Johnson, 2003; Parmar et al., 2006; Sohn et al., 2005). KLF2 mediates transcription of a large fraction of the endothelial anti-inflammatory, antithrombotic, and antioxidative genes. Endothelial KLF2 knockout (KO) mice are embryonic lethal due to high output heart failure caused by low peripheral resistance (Lee et al., 2006). In adults, KLF2 stabilizes the vasculature and limits vascular disease in the face of metabolic and inflammatory challenges (Jain et al., 2014).

LSS activation of the MEKK2/3–MEK5–ERK5 kinase cascade is critical in *Klf2* induction (Abe and Berk, 2014). By contrast, low and disturbed shear stress (DSS) induces KLF2 weakly, which contributes to atherosclerosis susceptibility at regions of DSS (Dekker et al., 2002). Conversely, reduction of *Klf2* expression by oxidized low density lipoprotein and hyperglycemia is thought to contribute to atherosclerosis (Birdsey et al., 2015;

Lee et al., 2013; Zhong et al., 2015). However, after more than a decade of study, how flow induces *Klf2* is incompletely understood.

We therefore used a CRISPR-Cas9 whole genome screen to identify genes regulating LSS stimulation of the *Klf2* promoter. Mechanistic analysis based on these results revealed that *Klf2* is induced via a branched pathway in which MEKK2/3–MEK5–ERK5 signaling is amplified by a mitophagy-associated scaffolding complex. Differential activation of the mitochondrial pathway accounts for the preferential *Klf2* induction by LSS relative to disturbed shear. Altogether, this study provides a unifying foundation for understanding many aspects of vascular health and disease.

Results

CRISPR whole genome screen

To identify regulators of *Klf2*, we first developed an immortalized mouse aortic endothelial cell (MAEC) reporter line stably

¹Yale Cardiovascular Research Center, Section of Cardiovascular Medicine, Department of Internal Medicine, School of Medicine, Yale University, New Haven, CT; ²Department of Biology, University of Padua, Padua, Italy; ³Department of Neurology, Columbia University Medical Center, New York, NY; ⁴Department of Medicine, Cardiovascular Research Institute, Case Western Reserve University, Cleveland, OH; ⁵Department of Pharmacology and Physiology, CNS Research Group, Faculty of Medicine, Université de Montréal, Montreal, Quebec, Canada; ⁶Department of Cell Biology, Yale University, New Haven, CT; ⁷Department of Biomedical Engineering, Yale University, New Haven, CT.

Correspondence to Brian G. Coon: brian.coon@yale.edu; Martin A. Schwartz: martin.schwartz@yale.edu.

© 2022 Coon et al. This article is distributed under the terms of an Attribution–Noncommercial–Share Alike–No Mirror Sites license for the first six months after the publication date (see <http://www.rupress.org/terms/>). After six months it is available under a Creative Commons License (Attribution–Noncommercial–Share Alike 4.0 International license, as described at <https://creativecommons.org/licenses/by-nc-sa/4.0/>).

expressing destabilized GFP (d2EGFP) driven by the 1.7 kb *Klf2* promoter (Fig. 1 a; and Fig. S1 a). As expected, LSS (18 dynes/cm²) induced the reporter $\approx 10\times$ (Fig. S1 b). These cells were transduced with a lentiviral CRISPR/Cas9 library targeting each protein-coding gene with six unique sgRNAs (Fig. 1 b; Shalem et al., 2014). Infected cells were stimulated with LSS at 18 dynes/cm² for 18 h and FACS-sorted into seven contiguous gates, approximating a normal distribution of reporter expression for controls (Fig. 1 c; and Fig. S1, d–f). 13 shear/FACS-sorting sessions, involving 280 parallel plate flow chambers, were used to stimulate, sort, and pool approximately 5×10^7 cells. Cells from each bin were subjected to limited PCR to recover and barcode the sg-sequences from the genome-integrated lentiviral cassettes (Fig. 1 b, blue arrows, and Fig. S1, g–i). Pooled DNA was subjected to Illumina sequencing and the counts for each uniquely barcoded sgRNA were tallied. *Klf2*:GFP induction scores were assigned by quantifying the area under the curves of observed-expected distributions. sgRNAs that induced a shift into low-expression gates indicated suppression of *Klf2* induction, exemplified by the positive control MEK5 (*Map2k5*) sgRNAs (Fig. 1 d). For each gene, the cumulative loss-of-function score was derived by summing the three sgRNA scores that diverged most from control (Fig. 1 e and Table S1). 370 genes decreased *Klf2*:GFP induction with Z scores >4 . To confirm these results, we analyzed LSS induction of endogenous *Klf2* after single CRISPR KO of select genes among the top 100 hits (Table S1). Approximately half of these lines significantly reduced *Klf2* with additional hits trending toward lower *Klf2* expression.

The MAPK pathway

The pathway upstream of the MEKK2/3–MEK5–ERK5 kinase cascade is poorly understood. We therefore focused on hits regulating the activity of these kinases. We first established a gel-shift assay for phosphorylation-dependent activation of MEKK2, MEKK3, and ERK5 (Fig. S2, a and b). LSS induced rapid, sustained activation of MEKK2 and MEKK3, whereas ERK5 activation showed a transient peak at ~ 20 min followed by a dip and then sustained activation beginning at ~ 3 h (Fig. S2, c–e). The reason for the transient drop in ERK5 activation between 45 min and 3 h is unknown. As expected, both MEKK2 and MEKK3 contribute to ERK5 activation (Fig. S2, f–h). Active ERK5 then translocates to the nucleus to induce gene expression in a MEK5-dependent manner (Fig. S2, i and j; Erazo et al., 2013).

Using the ERK5 gel-shift assay to examine the top hits from the CRISPR screen showed that MEK5 sgRNA completely blocked ERK5 activation, as expected (Table S2). The second most effective guide targeted the autophagy and signaling adaptor p62 (*Sqstm1*), followed by essential MCU regulator (EMRE/*Smdt1*) a critical regulator of the mitochondrial calcium uniporter (MCU). p62-KO and EMRE-KO also blocked ERK5 nuclear translocation (Fig. S2, k–n), confirming their upstream roles.

Role of p62

p62 (*Sqstm1*) is an adaptor protein involved in autophagy/mitophagy, ROS signaling, and polyubiquitinated protein processing (Sanchez-Martin and Komatsu, 2018). Interestingly, in

addition to ubiquitin- and LC3-binding domains, p62 contains a PB1 domain, a feature shared with MEKK2, MEKK3, and MEK5 (Fig. 4 a). PB1 domains mediate homophilic interactions via acidic-basic interfaces (Moscat et al., 2006). Indeed, tagged p62 colocalized and immunoprecipitated (IPed) with all members of the kinase module, most strongly MEK5 (Fig. S3, a and b). To understand the activation pathway, we sought to identify other components of this complex. Lysates from ECs expressing GFP-p62 and Flag-MEK5, with and without shear stress, were IPed with anti-Flag, eluted with Flag peptide, then re-IPed with GFP-TRAP to isolate only those proteins present in the specific complex. This procedure identified the p62-binding mitophagy proteins NIPSNAP1, NIPSNAP2, and TMEM160 as the strongest interactors (Fig. S3 c; Princely Abudu et al., 2019).

The involvement of Nipsnaps in mitophagy, in which damaged mitochondria are targeted for degradation, plus a role for EMRE in Erk5 activation and *Klf2* induction, pointed toward the involvement of mitochondrial metabolism and mitophagy. Indeed, gene set enrichment analysis of the ranked genes from the screen identified mitophagy and mitochondrial organization, along with shear stress signaling and oxidative stress signaling as key regulators (Fig. 1 f). We therefore examined LSS regulation of these pathways.

A mitochondrial remodeling pathway stimulated by LSS

We began by testing ROS, which are known to influence ERK5 activity (Abe et al., 1996). *N*-acetyl cysteine (NAC), a nonselective ROS quencher, and MitoQ, a mitochondria-specific quencher, each blocked shear-induced ERK5 activation (Fig. 2 a). We next assessed the origin of the ROS by targeting the ROS-sensitive GFP variant, roGFP, to different intracellular domains. These assays identified mitochondria as the principal source of shear-induced ROS (Fig. 2 b). Calcium entry via the MCU stimulates mitochondrial oxidative phosphorylation, which increases ROS production (Gherardi et al., 2020). To test the role of calcium, we treated cells with either the calcium chelator BAPTA-AM or the MCU inhibitor KB-R9743 (Santo-Domingo et al., 2007). Both blocked ROS production in response to shear (Fig. 2, c and d).

Mito-calcium and mito-ROS have the capacity to expand or deplete mitochondrial content through effects on mitochondrial fission and mitophagy (Scheitlin et al., 2016; Shirihai et al., 2015). We therefore assayed mitochondrial dynamics by fluorescence microscopy. Staining for the mitochondrial marker TOMM20 revealed that LSS triggered mitochondrial fragmentation (Fig. 2 e and Fig. S4 a). These mitochondrial fragments colocalize with the autophagy marker LC3b by 6 h of LSS (Fig. 2 f). Additionally, assaying mitochondrial content by quantitative PCR (qPCR) of the mitochondrial chromosome (mtDNA; Rooney et al., 2015) revealed that LSS initially increased mtDNA, which is often associated with calcium-induced fission (Lewis et al., 2016), followed by a subsequent decrease, consistent with mitophagy, resulting in below baseline levels by 18 h (Fig. 2 g and Fig. S4 b).

Mitochondrial damage triggers accumulation of the ubiquitin kinase PINK1, which phosphorylates Parkin and other targets to initiate mitophagy. PINK1 accumulation in the presence of

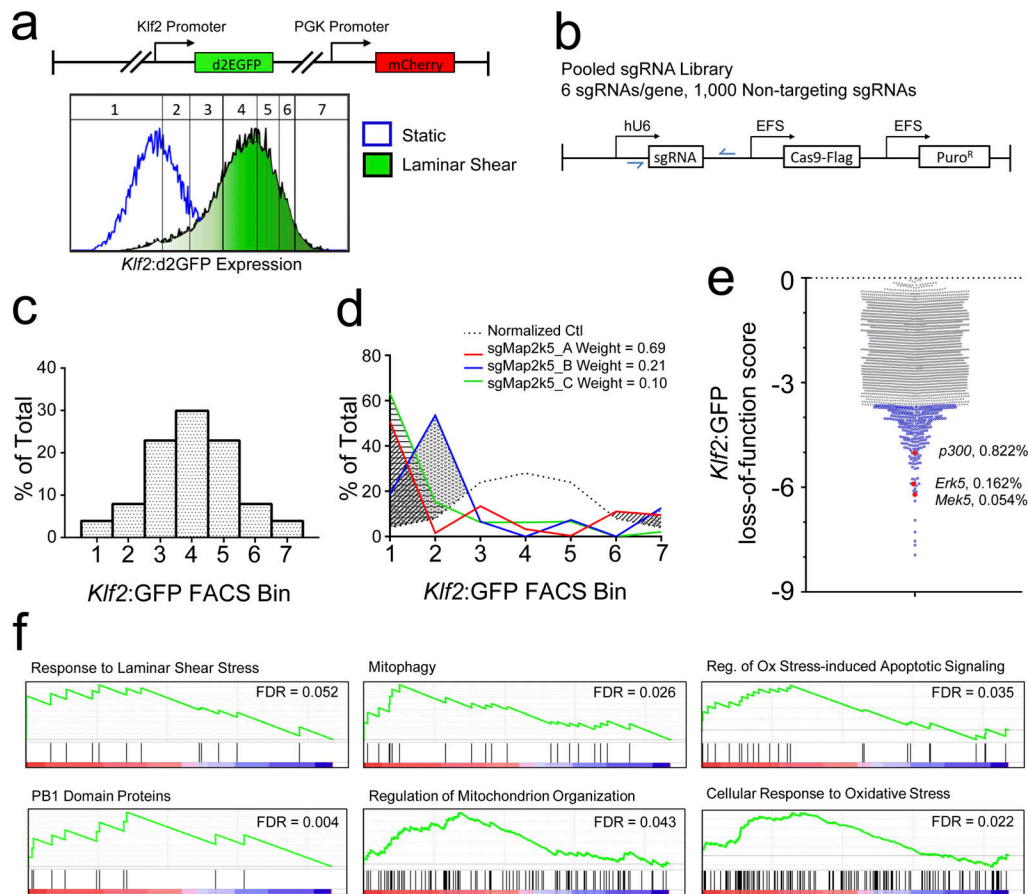


Figure 1. CRISPR screen to identify regulators of *Klf2* expression. (a) The lentiviral *Klf2*:GFP reporter expresses d2EGFP (half-life of ~2 h) driven by the *Klf2* promoter. The vector also contains mCherry controlled by the PGK promoter as an internal control. MAECs expressing the reporter showed a uniform, ~10-fold increase in green/red ratio after 16 h LSS. A distribution plot of the GFP/mCherry ratio (normalized GFP intensity) indicates approximate location of the FACS-sorting gates used for CRISPR screening. (b) Lentiviral vectors express Cas9 and one of 130,000 sgRNAs, with 6 sgRNAs targeting each gene and 1,000 nontargeting control sgRNAs via EFS and U6 promoters, respectively. (c) FACS gates were positioned according to GFP/mCherry percentiles to achieve a normal distribution. (d) *Mek5* sgRNAs induce a leftward shift in the distribution among gates compared to nontargeting sgRNAs, indicating reduced reporter expression. The shaded areas indicate the difference from control for each guide. These values were weighted by the relative abundance of each sgRNA. (e) Plot of Z scores for all genes ≤ 0 . Candidate genes among the lower fifth percentile are labeled in blue (complete list in Table S1). The positions of known *Klf2* regulatory genes *Erk5* (*Mapk7*), *Mek5* (*Map2k5*), and *p300* (*Ep300*) are labeled red along with their percentile ranking. (f) Gene set enrichment analysis of select pathways within the *Klf2*:GFP loss-of-function gene set. Component gene distributions and false discovery rates are shown for select pathways.

bafilomycin, which inhibits its degradation in lysosomes, is a measure of mitophagic flux (Yoshii and Mizushima, 2017). This assay showed increased PINK1 turnover after ~3 h of LSS (Fig. S4 c), again suggesting increased mitophagy. We therefore directly visualized mitophagy using mitochondrial-targeted mKeima (mito-Keima), a fluorescent protein that is differentially excited in neutral and acidic environments. Data confirm redistribution of mito-Keima into mito-lysosomes by ~3 h, which persists throughout the time course (Fig. 2 h).

We next examined the roles of EMRE and PINK1 in regulating mitochondrial content. Deletion of either gene blocked the effects of LSS, with deletion of PINK1 resulting in a large increase at later times, consistent with inhibition of mitophagy (Fig. 2 i). Additionally, we observed that PINK1 deletion also resulted in a marked decrease in lipidated LC3b accumulation (Fig. S4 d), suggesting that it regulates the shear-induced change in autophagic flux described previously (Vion et al., 2017). To further test the possibility that MCU activity is required for shear-

induced mitophagy, we tested the effect of the MCU inhibitor in mito-Keima-expressing human umbilical vein endothelial cells (HUVECs). Indeed, treatment mildly inhibited shear-induced mitochondrial turnover (Fig. S4 e). Together, these results define a pathway in which LSS-induced calcium elevation drives mitochondrial activation and mitochondrial homeostasis via mitophagy.

Mitochondrial regulation of ERK5

We then studied how this mitophagy pathway affects LSS-induced ERK5 activation and *Klf2* induction. As noted above, KO of the mitochondrial calcium uniporter subunit EMRE reduced ERK5 activation (by both gel-shift and nuclear translocation) and *Klf2* promoter induction by LSS (Fig. 3, a and b); however, it had no effect on MEKK2 activation (Fig. 3 c). Deletion of PINK1 also reduced ERK5 activation and *Klf2*:d2GFP induction by LSS without affecting MEKK2 activation (Fig. 3, d–f). These data suggest that transmission of the signal from

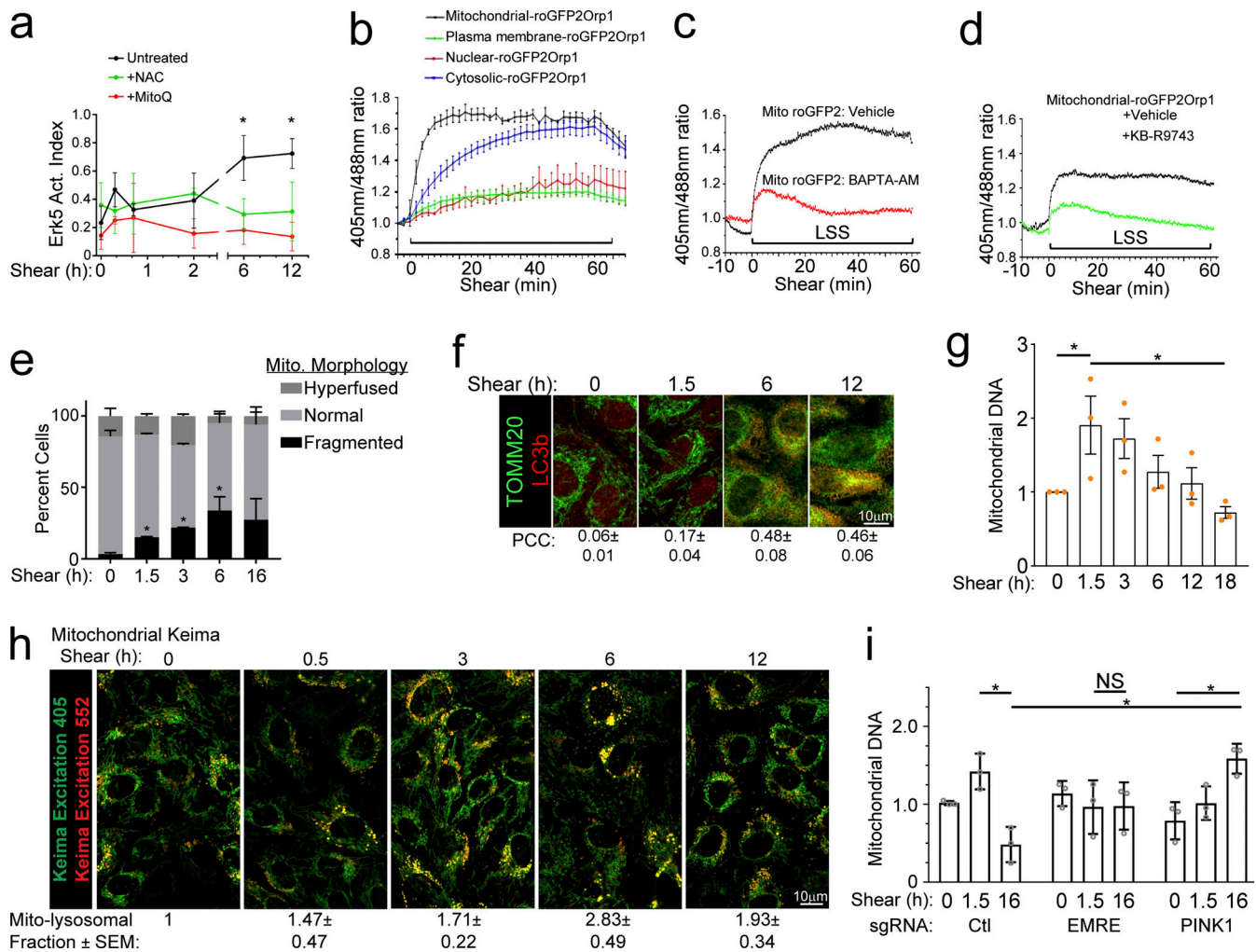


Figure 2. Lamellar shear-induced mitochondrial remodeling. (a) MAECs treated with 2 mM NAC or 2 μ M MitoQ were subject to 18 dynes/cm² LSS for the indicated times and ERK5 activation assayed by the Western blot and gel-shift assay. Values are means \pm SEM, $n = 3$. (b) HUVECs expressing the roGFP2 oxidative stress biosensor localized to the indicated compartments were subjected to 18 dynes/cm² LSS and fluorescence monitored. Values are means \pm SEM, $n \geq 6$. (c) HUVECs expressing the mito-*Grx1-Rogfp2* biosensor were treated with or without 5 μ M BAPTA-AM and subjected to 18 dynes/cm² LSS. Mitochondrial-roGFP fluorescence was monitored as in panel b. $N = 2$. (d) HUVECs expressing the mito-*Grx1-Rogfp2* biosensor with or without 10 μ M KB-R7943 were subjected to 18 dynes/cm² LSS and mitochondrial-roGFP fluorescence monitored as in panel b. $n = 2$. (e) LSS-stimulated HUVECs were fixed and stained for the mitochondrial marker TOMM20. Mitochondrial morphology was then scored in \sim 500 cells/experiment. $N = 3$ independent experiments. (f) HUVECs were exposed to LSS for the indicated times, fixed, and stained for LC3b and TOMM20. The fraction of cells exhibiting mitochondrial-LC3 colocalization was quantified by Pearson's Correlation Coefficient (PCC). Values are means \pm SEM; $n = 3$. (g) Shear-induced changes in HUVEC mitochondrial DNA content quantified by qPCR at the indicated times. $n = 3$. (h) HUVEC were transduced with mitochondrial-targeted mito-Keima, subjected to shear for the indicated times, and imaged by confocal microscopy. The 405- and 552-excited images represent the mitochondrial and mito-lysosomal fractions, respectively, which are quantified and represented as means \pm SEM; $n = 3$. (i) Control, EMRE^{-/-}, or PINK1^{-/-} MAECs were subjected to shear and mtDNA quantified by qPCR. Values are means \pm SEM, $n = 3$. *, $P < 0.05$ by one-way ANOVA or two-way ANOVA (i).

MEKK2/3 to ERK5 was affected. Using the aforementioned ROS quenchers and inhibitors of calcium signaling, we confirmed that mito-calcium and mito-ROS specifically enhance ERK5 activation without affecting MEKK2 activity (Fig. 3 g). We also tested the general role of autophagy using ULK1, PIKFYVE, and vATPase inhibitors, which impair autophagosome initiation, trafficking, and acidification, respectively. ULK1 and PIKFYVE inhibitors mildly reduced ERK5 activation and *Klf2*:d2GFP induction while vATPase inhibition showed no effect (Fig. S4, f-k). These results suggest that early events in triggering mitophagy rather than mitophagic flux are critical. While these

results support a role for Ca⁺⁺ stimulated mitophagy in the LSS pathway, direct stimulation of cytoplasmic Ca⁺⁺ without flow did not activate ERK5 (Fig. S4 l). Inducing mitophagy via mitochondrial damaging agents was also insufficient for ERK5 activation in the absence of flow (Fig. S4, m-p). Collectively, these data suggest that ERK5 activation and *Klf2* induction by LSS involves a two-pronged pathway involving both activation of MEKK2/3 and a mitophagy pathway that augments ERK5 activation but by itself is insufficient.

We validated these results in vivo by examining the endothelium in mouse aortas en face. We imaged regions of the

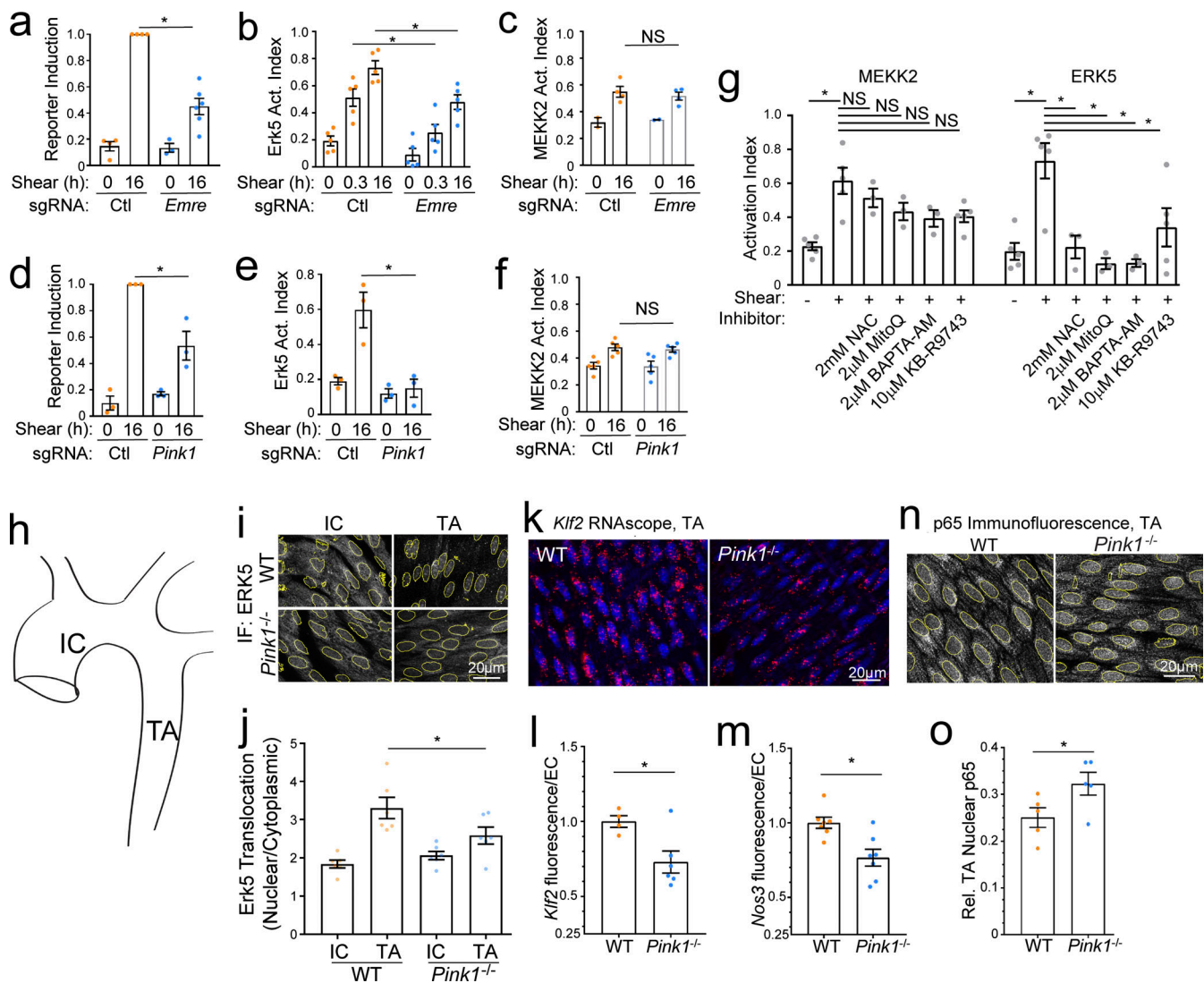


Figure 3. The mitochondrial pathway enhances ERK5 coupling. (a and d) *Klf2*:GFP reporter induction after 16 h LSS stimulation of control, EMRE-KO, or PINK1-KO cells assayed by immunoblot. (b and e) ERK5 activation index of control, EMRE-KO, and PINK1-KO cells stimulated with LSS for the indicated times. (c and f) MEKK2 activation index of control, EMRE-KO, and PINK1-KO cells stimulated with LSS for the indicated times, assayed by Western blot gel-shift. (g) MAECs treated with the indicated inhibitors were subjected to 16 h shear and assayed for activation of MEKK2 and ERK5. NAC, an antioxidant; MitoQ, a mitochondrial-targeted antioxidant; BAPTA-AM, a calcium chelator; KB-R9743, an inhibitor of the mitochondrial calcium uniporter. $n = 3$ or 5 for KB-R9743. (h) Mouse arterial endothelium was examined in the IC of the ascending aorta and the straight portion of the TA. (i and j) Aortas from WT and PINK1-KO mice were stained for ERK5 (i) and the endothelium was imaged en face (j) before quantifying mean nuclear translocation in the IC and TA. $n = 5$. (k and l) *Klf2* mRNA within TAs of WT and PINK1-KO mice was labeled using RNAscope, counterstained with DAPI, and imaged en face. *Klf2* mRNA labeling show as red speckles. (l) Normalized average fluorescence intensity per EC per mouse is shown. $n = 6$ WT and 6 PINK1-KO mice. (m) eNOS mRNA expression in the TA was labeled by RNAscope and quantified as in l. (n and o) Endothelial p65 immunostaining was examined in the TA and nuclear translocation quantified. $n = 5$ WT and 5 PINK1-KO mice. *, $P < 0.05$ by one-way ANOVA except l-o, which used Student's *t* test.

thoracic aorta (TA), where high, laminar shear induces *Klf2*, and the inner curvature of the arch (IC), where shear is low and disturbed, and *Klf2* is low (Fig. 3 h; Hahn and Schwartz, 2009). Assaying ERK5 activation by quantifying its nuclear localization showed higher translocation in the TA than the IC in WT aortas, as expected (Fig. 3, i and j). PINK1-KO mice demonstrated weaker ERK5 translocation in the TA region, supporting a role for mitophagy in ERK5 activation under LSS in vivo. However, there was no significant difference in the IC, a region of low/disturbed flow. Measuring *Klf2* expression by RNAscope in situ hybridization showed that PINK1-KO aortas also have

reduced expression of both *Klf2* (Fig. 3, k and l) and its critical target gene *Nos3* (eNOS; Fig. 3 m). KLF2 and eNOS suppress NF- κ B transcriptional activity and pro-inflammatory signaling (Das et al., 2006). We therefore assayed NF- κ B activation by measuring its nuclear translocation. PINK1-KO TA endothelium had higher nuclear p65 than WT counterparts (Fig. 3, n and o). This effect was again seen in the TA that is under high, unidirectional shear stress but not in the IC under low/disturbed shear. We conclude that LSS-induced mitophagy enhances ERK5 activation, *Klf2* induction, and endothelial function in vitro and in vivo.

p62 stabilizes the MEKK2/3–MEK5 complex

We next sought to understand how mitophagy enhances LSS-induced ERK5 activity. The MEKK2 and MEKK3 PB1 domains contain a basic patch (Type II), which binds the acidic patch on MEK5's PB1 domain (Type I). However, p62's PB1 domain contains both acidic and basic patches (Type I/II), enabling it to bind both subtypes (Lamark et al., 2003; Nakamura et al., 2010). To test the role of PB1 interactions, we rescued p62-KO with both WT p62 and a mutant in which the basic patch was neutralized (KRR-to-AAA) to block binding to type I PB1 domain proteins, including MEK5 (Fig. S3 d; Ciuffa et al., 2015; Lamark et al., 2003; Nakamura et al., 2010). WT but not mutant p62 rescued shear-induced *Klf2*:GFP (Fig. 4 b). Thus, association with MEK5 is required for its function.

While performing these experiments, we noticed that LSS promoted p62/Sqstm1 accumulation beginning at about 4 h and reaching 10–30-fold by 16 h (Fig. S3 e). The *Sqstm1* gene is induced by the oxidation-reduction (REDOX)-sensitive transcription factor, NRF2, which is strongly activated and upregulated by LSS (Fig. 4 c and Fig. S3 f; Jain et al., 2010; Zakkar et al., 2009). NRF2-KO partially reduced LSS-induced p62 accumulation (Fig. 4 c), suggesting p62 upregulation by LSS via both an NRF2-dependent transcriptional mechanism and a post-transcriptional mechanism.

p62 is held as an inactive dimer, which is activated by binding to ubiquitinated cargo (Isogai et al., 2011; Long et al., 2010). Mitophagy is initiated by ubiquitination of the mitochondrial surface downstream of PINK1 (Geisler et al., 2010). We therefore hypothesized that mitochondrial ubiquitination leads to activation of p62 via binding to its ubiquitin-associated (UBA) domain, which relieves autoinhibition. Active p62 then promotes ERK5 activation. To test conformational activation of p62, we developed a novel assay using a p62 antibody that is raised against a region of the p62 UBA domain that is involved in autoinhibition (Long et al., 2010). We predicted that this antibody may preferentially recognize active p62. Indeed, IP of EC lysates showed that LSS triggered a strong increase in p62 in the IP within 20 min, which required ROS (Fig. 4 d). Additionally, our functional data showed that p62-KO did not detectably affect the MEKK2 gel shift (Control = 0.54 ± 0.04 , p62-KO = 0.57 ± 0.04). Together, these data show that LSS activates p62, which contributes to the activation of ERK5 and induction of *Klf2* but not MEKK2. This places p62 in the mtCa⁺⁺/mito-ROS/mitophagy arm of the ERK5 pathway.

p62 colocalizes with both endogenous MEK5 and MEKK2 in cytoplasmic punctae (Fig. S3 a). We further interrogated these structures' dynamics under shear and their relationship to mitochondria using the mitochondrial marker mCHERRY-FIS1^{TMD} (Allen et al., 2013). LSS increased both the number of p62-positive punctae, its colocalization with MEK5 (Fig. 4, e and f) and colocalization with mCHERRY-FIS1^{TMD} (Fig. 4, e and g). Cell fractionation showed that MEK5 translocates from the cytosol (100,000 g supernatant) into a mitochondrial-enriched fraction (10,000 g pellet), which was blocked by p62-KO or NAC treatment (Fig. 4 h). No changes in the abundance of MEK5 in other fractions were observed. Lastly, we directly tested p62's role in assembly of the kinase complex by IP of MEKK2 with GFP-

MEK5. KO of p62 completely blocked the LSS-stimulated association between MEK5 with MEKK2 (Fig. 4 i).

To validate these results in vivo, we examined the endothelium in p62-KO mice. As expected, p62 deficiency reduced ERK5 nuclear translocation in the TA but not the IC (Fig. 4 j). Next, we measured expression of *Klf2* and its target gene *Nos3* using RNAscope. *Klf2* expression in the TA was reduced by about 30% and *Nos3* reduced by about 50% (Fig. 4, k and l). Altogether, these data reveal that LSS-induced oxidative stress and mitophagic signaling activates p62 to stabilize the MAPK cascade upstream of *Klf2*, as summarized in Fig. 4 m.

A role for PIEZO1, a mechanosensitive calcium channel

The mechanosensitive ion channel PIEZO1 is implicated in both calcium entry into cells and LSS mechanotransduction, including induction of *Klf2* (Duchemin et al., 2019; Li et al., 2014; Ranade et al., 2014; Wang et al., 2016). The calcium-dependent activation of mitochondria therefore prompted us to investigate PIEZO1 in this pathway. KO of PIEZO1 (Fig. S5 a) markedly reduced the activation of ERK5 and induction of *Klf2* by LSS (Fig. S5, b and c). However, PIEZO1-KO had no effect on LSS activation of MEKK2 (Fig. S5 b). PIEZO1 is thus required for the mitochondrial arm of the pathway. However, as for other mitochondrial inputs, activation of PIEZO1 by its agonist Yoda had no effect in the absence of LSS (Fig. S5 d).

Laminar vs. disturbed shear stress signaling

Data from us (Fig. 5 a) and others (Chappell et al., 1998) show that *Klf2* is induced more strongly by LSS compared to disturbed shear, generally modeled in vitro by oscillatory shear stress (OSS). Interestingly, our analysis of PINK1- and p62-KO mice showed that these deletions reduced *Klf2* expression in regions of high LSS but not in regions of disturbed shear. As the cause of differential *Klf2* expression under LSS vs. OSS is unknown, we investigated further. To our surprise, OSS (1 ± 3 dynes/cm²) activated MEKK2 as well as LSS, despite strongly impaired ERK5 activation (Fig. 5, b–d). Although mitochondrial fragmentation was similar between cells stimulated with either LSS or OSS (Fig. 5 e), mtDNA was not cleared after OSS, suggesting a mitophagy defect (Fig. 5 f). This was confirmed using mito-Keima (Fig. 5 g). Analysis of mitophagy in vivo using LC3-GFP transgenic mice stained with anti-GFP and anti-TOMM20 antibodies showed ~3× more double-positive autophagosomes in the TA endothelium than the IC (Fig. 5 h). Western blotting for NRF2 and p62 showed that OSS upregulated both NRF2 and p62 less well than LSS (Fig. 5, i and j). OSS also stabilizes the MEKK2–MEK5 complex less well than LSS (Fig. 5 k). OSS thus activates MEKK2/3 but induces *Klf2* less well due to dysregulated mitophagy and impaired assembly of the p62-kinase complex.

PINK1 facilitates vascular remodeling in vivo

FSS-driven vascular remodeling that restores perfusion in the face of vessel restrictions is a major mechanism that opposes coronary and peripheral artery disease and mediates recovery from myocardial infarction (Faber et al., 2014; Heil and Schaper, 2004). KLF2 and downstream targets such as eNOS are critically important in this process (Caradu et al., 2018; Krause et al., 2018;

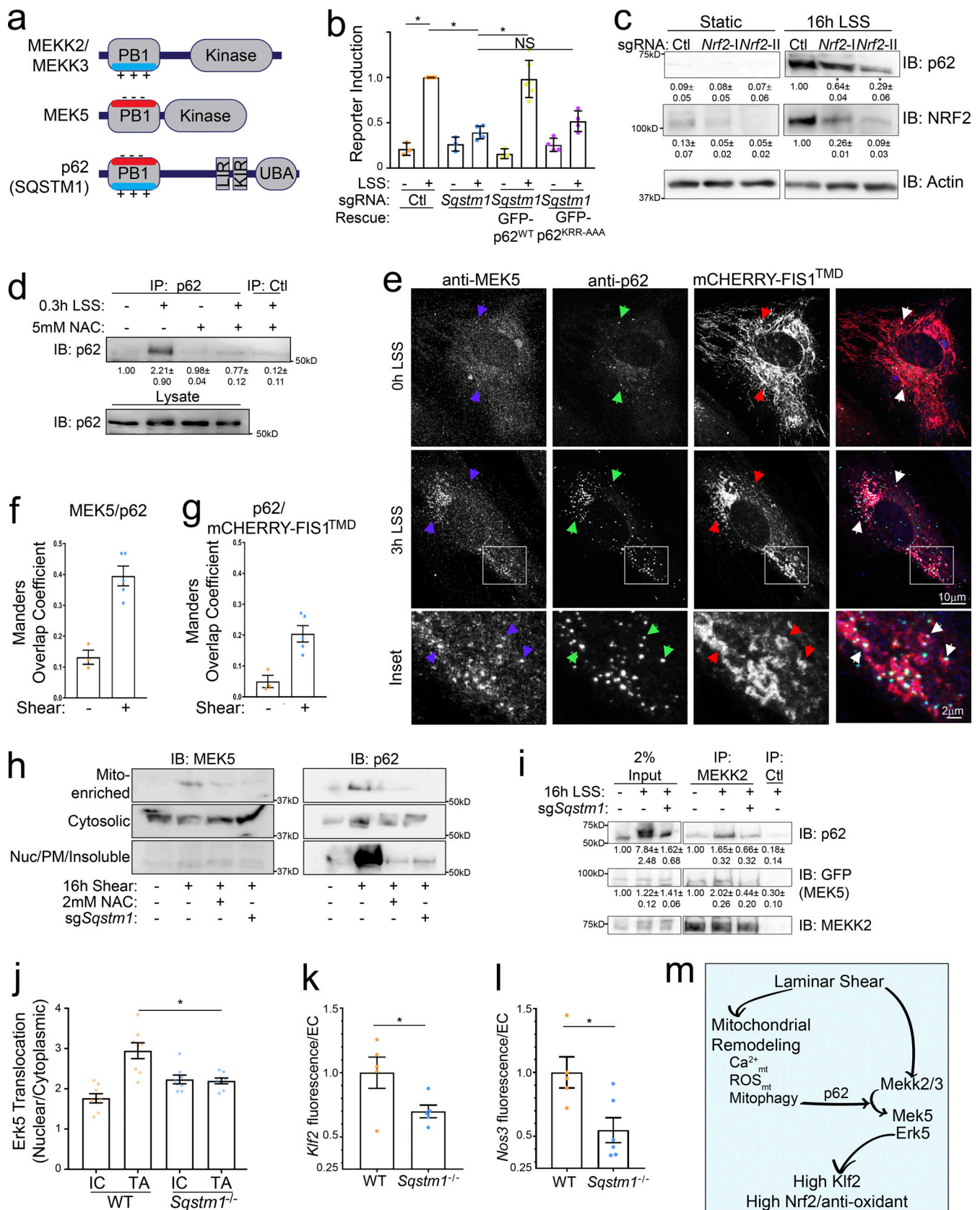


Figure 4. **p62 is activated by LSS and enhances *Klf2* induction.** (a) Domain organization of MEKK2/3, MEK5, and p62. MEKK2/3 has Type II PB1 domains whereas MEK5 has a Type I PB1 domain. p62 has a Type I/II PB1 domain, KEAP1 and LC3 binding sites (KIR and LIR), and a ubiquitin binding domain (UBA). (b) Control or p62-KO MAECs were reconstituted with sgRNA-resistant p62^{WT}-GFP or p62 with a mutant PB1 domain basic patch (p62^{KRR-AAA}-GFP) and

assayed for *Klf2*:GFP induction by LSS. Data points represent summary data from biological replicates. **(c)** MAECs were transduced with control or *Nrf2* sgRNAs and stimulated with 16 h LSS. Lysates were then immunoblotted for p62, NRF2 and actin. Quantified values are means \pm SEM; $n = 3$. **(d)** MAECs were treated with LSS and/or NAC as indicated. Active p62 was then purified with an anti-p62-UBA antibody and quantified by immunoblotting. Representative blots and quantification from three independent experiments are shown. **(e)** HUVEC transduced with the mitochondrial marker, mCHERRY-FIS1^{TMD}, were subjected to shear, fixed, and stained for p62 and MEK5. **(f and g)** The Mander's overlap coefficients of MEK5 colocalizing with p62 (f) and p62 colocalizing with mCherry-FIS1^{TMD} (g) were quantified. Values are means \pm SEM of individual imaging fields from a representative experiment. **(h)** MAECs transduced with nontargeting or *Sqstm1*-KO sgRNAs were treated with LSS and/or NAC as indicated. Cells were fractionated and fractions immunoblotted for MEK5 and p62. Representative immunoblots and quantification ($n = 3$) are shown. **(i)** MAECs were transduced with GFP-MEK5 with or without *Sqstm1*-KO sgRNAs as indicated. Cells were subjected to shear, MEKK2 IPed, and IPs probed by immunoblotting. MEKK2, p62, and GFP-MEK5 were quantified by band densitometry, $n = 3$. **(j)** Aortas from WT and *Sqstm1*^{-/-} mice (eight each) were stained en face for ERK5 and nuclear translocation was measured within the IC and TA as in Fig. 3 j. Average translocation index per region per mouse is shown. **(k)** TAs of WT vs. *Sqstm1*^{-/-} mice were stained for *Klf2* mRNA using RNAscope and expression in ECs quantified as in Fig. 3 l. Normalized average fluorescence intensity per EC per mouse is shown. $N = 5$ WT and 5 p62-KO mice. **(l)** TAs were subjected to Nos3 RNAscope and quantified as in Fig. 3 m. $N = 4$ WT and 6 p62-KO mice. **(m)** Model for laminar shear stress regulation of ERK5 signaling through parallel pathways converging on the MEKK2/3–MEK5 complex. *, $P < 0.05$ by one-way ANOVA (b, c, and j) or Student's *t* test (k and l). Source data are available for this figure: SourceData F4.

Murohara et al., 1998; Yu et al., 2005). We therefore assayed the effect of inhibited mitophagy in PINK1-KO mice using recovery from hindlimb ischemia following femoral artery ligation to model these processes. Mice were subjected to a mild form of hindlimb ischemia as described in Materials and methods. Laser Doppler imaging to measure superficial perfusion after surgery (Fig. 6, a and b) showed impaired recovery in PINK1-KO mice. Imaging arteries at 14 d by microCT revealed substantially reduced vessel networks with smaller artery diameters in the thigh, where changes are driven primarily by elevated flow (example images and quantification in Fig. 6, c and d). Arteries in the calf, where VEGF-driven angiogenesis is more important, also showed fewer large-diameter arteries in PINK1-KO mice, though the effect was less pronounced. The lower levels of *Klf2* and *Nos3* in PINK1-KO mice thus correlate with defective flow-dependent arterial remodeling.

Discussion

Collectively, these results reveal that LSS stimulates *Klf2* expression through a two-armed pathway. One arm activates MEKK2/3 while the other activates mitochondria, resulting in mitophagy. These two pathways then converge upon a p62–MEKK2/3–MEK5 complex to optimally stimulate *Klf2* expression (Fig. 4 m). Anti-inflammatory LSS and pro-inflammatory OSS differ mainly in the mitochondrial arm of the pathway. Curiously, OSS initiates mitochondrial fragmentation but not mitophagy or assembly of the p62-dependent scaffolding complex. We suspect that OSS may interfere with the mitophagy pathway, but this remains unknown.

We think it noteworthy that the shear-stimulated mitochondrial oxidative stress pathway is counter-balanced not only by clearance of damaged mitochondria through mitophagy but also by a robust antioxidant response, marked by NRF2 induction (Fig. 4 c and Fig. S4 f). Mitophagy and antioxidant responses should suppress ROS-mediated inflammation (Ahmed et al., 2017; Zakkar et al., 2009; Zhang et al., 2014). Additionally, components of the pentose phosphate pathway (*Aldoa*, *Pgd*, *Tkt*), another REDOX homeostasis pathway, are well represented among the CRISPR screen hits (Table S1). Moreover, recent studies have shown that laminar shear influences mitochondrial-REDOX signaling to confer proper

responses, including KLF2 expression (Kant et al., 2022; Yamamoto et al., 2020). These data suggest that a delicate balance of pro- and antioxidative stress signaling determines activation of ERK5–*Klf2* vs. pro-inflammatory pathways (Liu et al., 2003).

Importantly, the mitochondrial arm provides a likely point of intersection for metabolic risk factors in atherosclerosis. Both hyperglycemia and hyperlipidemia suppress *Klf2* (Birdsey et al., 2015; Lee et al., 2013; Zhong et al., 2015) and autophagy (Liang et al., 2015; Weikel et al., 2015). Autophagy in turn facilitates *Klf2* activation and protects against artery disease (Vion et al., 2017). AMPK, a major activator of autophagy, is suppressed by overnutrition and implicated in activation of ERK5 and *Klf2* (Young et al., 2009). Thus, joint regulation of *Klf2* by a kinase cascade and a mitochondrial pathway provides a framework for future work aimed at understanding how metabolic and biomechanical factors determine artery disease.

These ideas suggest that the Erk5–*Klf2* pathway is an example of hormesis, by which mild stresses, in this case, increased ROS due to mitochondrial activation, induces adaptive responses that benefit the organism. More severe stresses, however, can overwhelm the system or interfere with the adaptive mechanism. Disturbed shear induces high levels of ROS, for example (Chatterjee and Fisher, 2014). We speculate that elevated ROS or other stresses from systemic risk factors may target components of the Erk5–*Klf2* pathway to reduce anti-inflammatory responses. Reliance on ROS to regulate gene expression may therefore confer disease susceptibility under unfavorable conditions.

Major unanswered questions include how flow activates MEKK2/3, the architecture and regulation of the p62-kinase scaffolding complex, why mitophagy but not bulk autophagy facilitates ERK5 activation and *Klf2* induction, why OSS fails to activate mitophagy, how metabolic factors influence this pathway, and how pathological metabolic effects can be overcome.

Materials and methods

Cells and cell culture reagents

HUVECs were obtained from the Yale Vascular Biology and Therapeutics core and cultured in Vasculife endothelial cell media (LL-0003; Lifeline Cell Technology). Experiments were

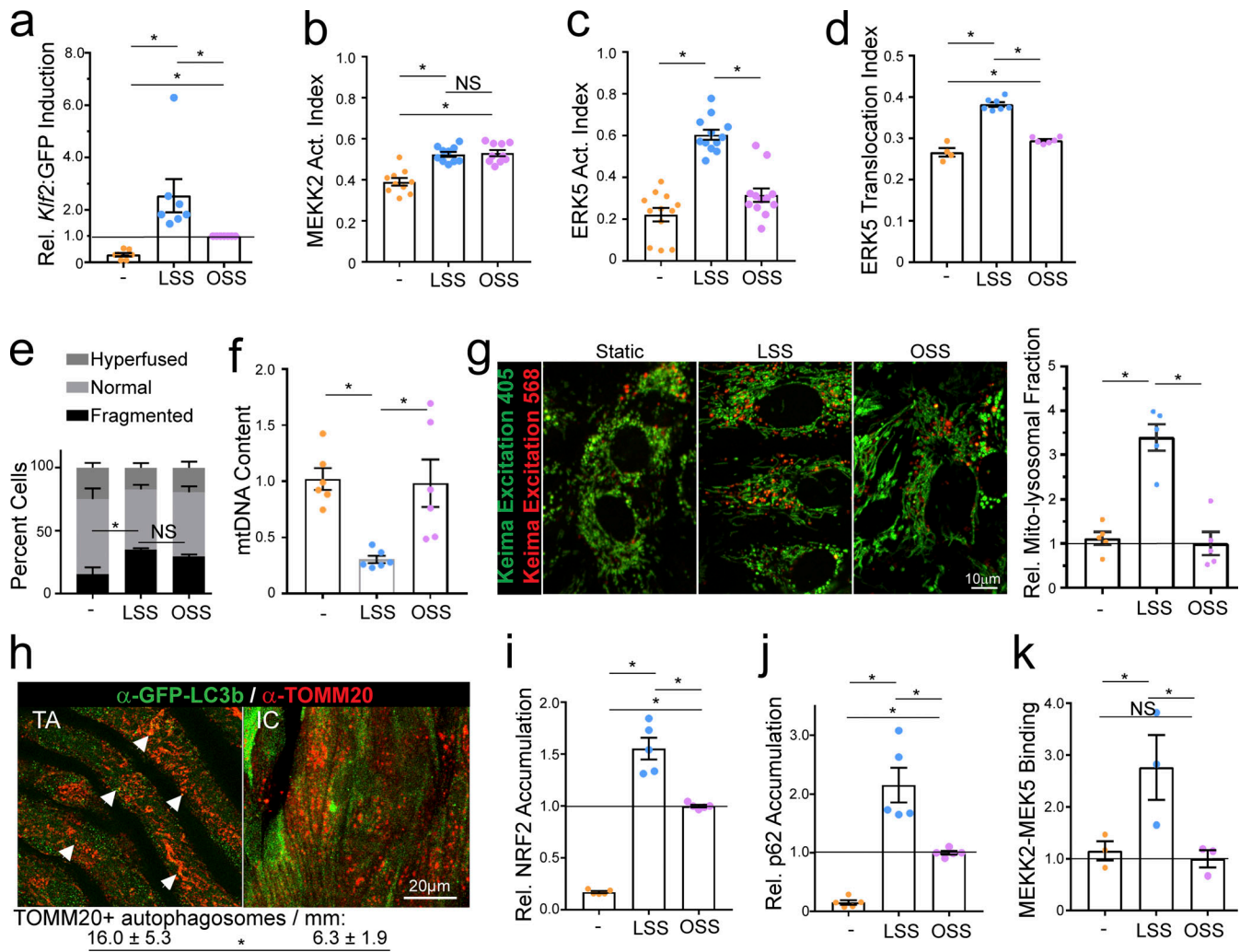


Figure 5. The mitochondrial pathway distinguishes high laminar from low/disturbed shear stress. (a) *Klf2*:GFP reporter MAECs were exposed to either 18 dynes/cm² LSS or 1 ± 3 dynes/cm² OSS for 16 h. (b–d) We then assayed GFP reporter levels, MEKK2 and ERK5 gel-shift (b and c), and ERK5 nuclear translocation (d). Values are means ± SEM; n = 7–11. (e) HUVECs were exposed to LSS or OSS for 16 h and mitochondrial fragmentation was assayed as in Fig. 2 e. (f) HUVECs were exposed to LSS or OSS for 16 h and mitochondrial DNA assayed as in Fig. 2 h. (g) HUVECs were transduced with mito-Keima and stimulated with LSS or OSS for 12 h before imaging as in Fig. 2 i. The mean mito-lysosomal fraction was quantified and graphed as means ± SEM with OSS normalized to 1.0; n = 5 independent experiments. (h) Aortas from adult GFP-LC3b transgenic mice were fixed, stained for GFP and TOMM20, and imaged en face to visualize ECs within the IC and TA. Confocal stacks were obtained and discrete LC3b+/TOMM20+ objects were counted. Images show representative 63× fields; quantified values (below) are means ± SEM, n = 4. (i and j) MAECs were exposed to either 18 dynes/cm² LSS or 1 ± 3 dynes/cm² OSS for 16 h before immunoblotting for NRF2 and p62; quantified values are means ± SEM with OSS normalized to 1.0; n = 5. (k) MEK2 was immunoprecipitated from cells stimulated with LSS or OSS, and associated MEK5 assessed by immunoblotting. Quantified results from independent experiments are shown as means ± SEM with OSS normalized to 1.0; n = 3. *, P < 0.05 by one-way ANOVA or Student's t test (h).

performed between passages 2–6 from multiple preparations of random donors. To isolate aortic endothelial cells from C57Bl/6j mice, the aorta was dissected and ringlets cultured on Matrigel droplets in Complete EC Medium (M1166; Cell Biologics; Ni et al., 2014). After purification, MAEC were immortalized with PyMT (22305; Addgene). This line was used to create the *Klf2* promoter reporter line. The *Klf2* promoter reporter encodes d2EGFP under the control of the 1.7 kb *Klf2* promoter and mCherry under the control of a constitutive PGK promoter. The 1.7-kb fragment encompasses the most prominent regulatory elements (Kumar et al., 2005). mCherry serves as an internal positive control for normal gene expression and protein turnover. The d2EGFP has a

2-h half-life (Zhao et al., 1999) to reduce basal GFP expression and improve signal to noise in dynamic systems. KLF2 protein has a similar half-life compared to the d2EGFP, indicating that the expression dynamics of the reporter are physiological (Wang et al., 2013). After transduction, a uniform *Klf2* reporter line was obtained by sequential FACS-sorting over a series of passages using narrow gates for (1) high mCherry, (2) low resting d2EGFP, and (3) high shear-induced d2EGFP.

CRISPR library screening

Mouse KO sgRNA libraries (10000000052; Addgene), encoding 65,000 sgRNAs apiece (Shalem et al., 2014), were transformed

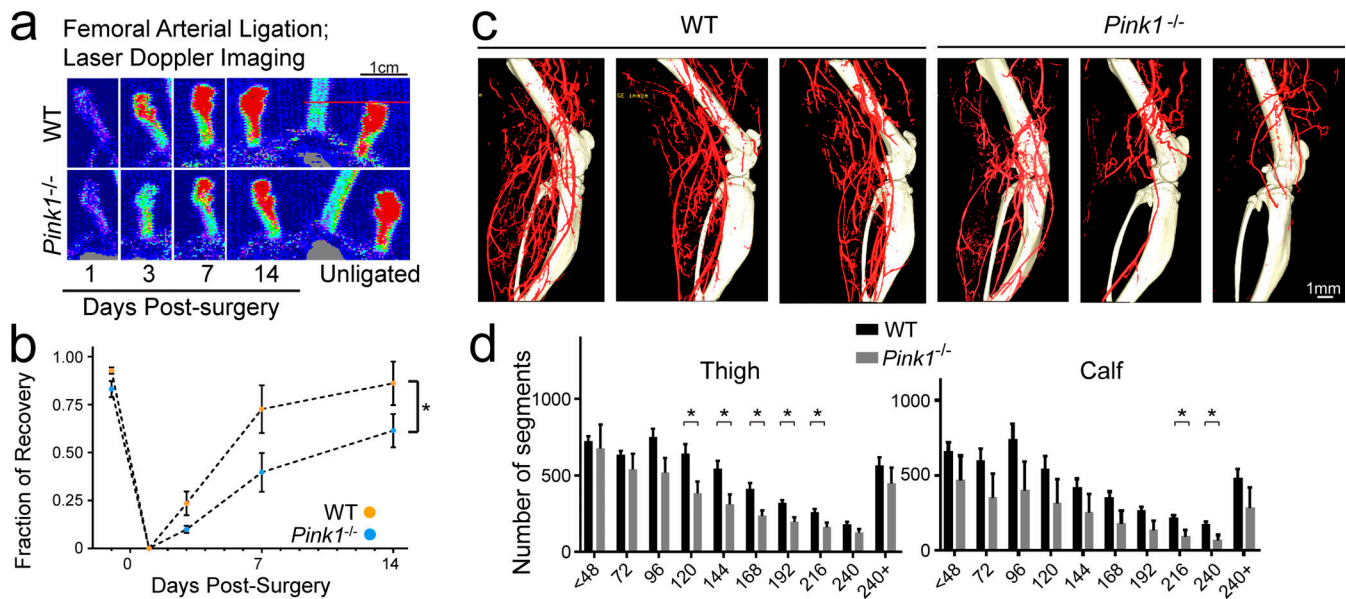


Figure 6. **Arterial remodeling.** (a) WT and PINK1-KO male mice were subjected to femoral arterial ligation and superficial blood flow measured by laser Doppler imaging at -1, +1, +3, +7, and +14 d. Representative images are shown. (b) Quantification of blood flow; values are means \pm SEM. $N = 5$ WT and 7 PINK1-KO mice. *, $P = 0.05$ by paired Student's t test. (c) 14 d after femoral arterial ligation, hindlimbs were subjected to microCT imaging. Representative images are shown. (d) Vessel segments intersecting with Z-planes running through the thigh and calf regions were counted and binned according to their cross-sectional diameters. $N = 5$ WT and 7 PINK1-KO mice. *, $P < 0.05$ by Student's t test.

into about 6,500,000 colonies (100 \times expansion) and plasmid maxi-prepped. Virus was produced by cotransfecting into 4×10^7 293T cells ($\approx 600\times$ expansion) with pMD2.G and psPAX and collecting supernatant at 60 and 84 h. Virus was titered to near 1 multiplicity of infection (MOI), confirmed by transducing a small number of MAEC and staining with anti-Cas9 (632607; Takara). Puromycin kill curves were generated to ensure that these cells remained insensitive. 10–20 d before the shear stress assays, *Klf2*-reporter MAEC were transduced at 1 MOI (infects $\sim 40\%$ of the population) and 3 d later subjected to minimal puromycin selection for 3 d. 2 d before shear stimulation, cells were seeded onto 10 $\mu\text{g}/\text{ml}$ fibronectin-coated plastic slides cut from 15-cm cell culture plates (353025; Falcon). Cells were then stimulated with 18 dynes/cm² laminar shear stress in one of five replicate parallel plate flow systems (Conway et al., 2017) for 18 h. Immediately after stopping flow, cells were rinsed with 4 $^\circ\text{C}$ PBS and lifted within 5 min in Accutase + 0.25% Trypsin + EDTA. Trypsin was quenched with 4 $^\circ\text{C}$ PBS + 2% FBS + soybean trypsin inhibitor and cells from replicate chambers/stations were pooled in ice-cold FACS sorting buffer. Sorting began within 30 min in a BD FACSaria fitted with 200 mw 488 and 532 lasers. As only four gates can be collected simultaneously, we first set two for the max/min four percentile of d2EGFP expressors (expressing normal levels of mCherry), the third gate for the next lowest eight percent of cells, and the fourth gate for the intermediate 84% of cells (See Fig. S1, d–f). Then after finishing, we resorted the fourth tube to resolve the four remaining gates (Fig. S1, e and f, right panels). We recovered 1–1.5 $\times 10^7$ cells for each of the sgRNA libraries to yield about 150–200 \times oversampling of each component sgRNA. Cells were pelleted and frozen at -80°C .

Library prep and next-gen sequencing

Genomic DNA from each of the FACS gates was spiked with 5 μg salmon sperm DNA and prepped with QiaAmp DNA extraction columns. Then, the integrated sgRNAs were extracted by performing limited PCR reactions in 320 wells per gate for each of the two sgRNA libraries, using Phusion DNA polymerase (NEB; [95 $^\circ\text{C}$ 30 s, 55 $^\circ\text{C}$ 40 s, 72 $^\circ\text{C}$ 20 s] $\times 20$ cycles). The reactions were re-pooled and amplicons concentrated/purified using AMPure resin (Beckman Coulter). Briefly, PCR reactions were mixed with 20% polyethylene glycol in 2.5 M NaCl, bound to resin for 15 min at room temperature, and washed twice with 70% ethanol before drying and elution. Eluted amplicons were then resolved by agarose electrophoresis (Fig. S1 g). Next, a second and third round of PCR was performed to attach the FACS gate/random barcodes and Nextera sequencing oligos (Illumina), respectively (Fig. S1, h and i). Ampure purification was performed after each PCR. Libraries were then mixed at equimolar ratio and subjected to 75 bp sequencing on a HiSeq2500 (Illumina).

Klf2 loss-of-function phenotype determination

Reads with mutations or indels in the conserved regions of the lentiviral cassette were excluded; for the remaining ($\approx 95\%$), sgRNA sequences, gate barcodes, and random barcodes were extracted, and replicate reads then removed. Once each of the libraries had been sufficiently sampled, we determined that there were 1–3 unique sgRNA inserts for each sorted cell, confirming low MOI (Fig. S1 j). The distribution of total counts for each of the library's sgRNAs reveals that 88% were detected at least 50 times, which we established as a cutoff for sufficient sampling (Fig. S1 k). Then, the normalized distribution and weighted sum (a composite of the distribution profile as

displayed in Fig. 1d) were determined by multiplying each bin's count by a weighted value, which is the ratio of expected vs. observed frequency, and summing these values across all gates. The average score of the nontargeting control sgRNAs was -0.024 and -0.07 for each library, respectively. Then, for each gene target, we selected each of the lowest scoring sgRNAs (loss-of-function) from each library and the next lowest scoring sgRNA, selected from between the two libraries, to have three unique sgRNAs for each gene. The Z scores for each were then summed, filtered for genes expressed in the endothelial transcriptome (Fang et al., 2017), and ranked (Fig. 1e). We similarly summed low scoring nontargeting sgRNAs, selected from random groups of six of the 1,000 embedded within the libraries. 5% of those nontargeting groups scored below $Z = -2.5$, while 1% scored below $Z \approx -3.8$ (Fig. S11).

Mice, aortic dissection, and en face preparation

Procedures were approved by the animal ethics committee of the Université de Montréal or the Yale University Institutional Animal Care and Use. All efforts were made to minimize animal suffering. WT, *PINK1*^{-/-}, and *SQSTM1*^{-/-} mice (Akundi et al., 2011) were bred on a C57Bl/6J background as heterozygotes. About 12–16-wk WT and *PINK1*^{-/-} and *SQSTM1*^{-/-} littermates were anesthetized and perfusion fixed with 4% PFA through the left ventricle. The heart and spinal column, with aorta attached, were then removed and fixed under gentle agitation for an additional 24 h at room temp. The aortas were dissected and the adventitia was removed. The middle segment of the thoracic aorta, between the fifth and eighth intercostal arteries, was excised and bisected longitudinally. The aortic arch was also bisected through the inner curvature and around the brachiocephalic, carotid, and subclavian arteries in the outer curvature side. After RNAscope or immunohistochemistry, these segments were mounted on slides, endothelium side-up, in Fluoromount.

Hindlimb ischemia, laser Doppler imaging, and microCT quantification

Mice were anesthetized and operated with a mixture of 1.5–2% isoflurane. The front hair of the right thigh was removed with Nair lotion and the local surgical area was disinfected. A 5-mm longitudinal skin incision was made in the right thigh. The distal femoral artery, proximal to the popliteal artery and saphenous artery, was explored and dissected. 6–0 silk sutures (Syneture) were used for the ligation before excision of the arterial vessel bed between the distal end of the superficial epigastric artery and the trifurcation of the femoral artery into the descending genicular, popliteal, and saphenous branches. The venous structures and accompanying peripheral nerves were kept intact. The overlying skin was closed with a 6–0 prolene (Ethicon) and disinfected. At the end of the procedure, Buprenorphine was administered subcutaneously at 0.05 mg/kg, once pre-emptively, then every 12 h for 72 h. The survival rate for this surgery was 100%.

Hindlimb perfusion was assessed noninvasively in the plantar foot before, 1, 3, 7, and 14 d after femoral ligation by scanning laser Doppler (model LDI2-IR modified for high resolution; Moor Instruments). The hindquarters were placed on the

top of a heater pad during scanning to minimize variation in body temperature. Doppler perfusion of the plantar foot was assessed within anatomically defined regions of interest (ROIs; Moor Instruments). The ROI for the plantar foot consisted of the hind paw margins. Procedures for minimal preparation, scanning, and ROI selections have been described in detail previously (Zhuang et al., 2011). Low or no perfusion is displayed as dark blue, whereas the highest degree of perfusion is displayed as red. These images were quantitatively converted into histograms that represented the amount of blood flow on the x-axis and the number of pixels on the y-axis in the traced area. The average blood flow in each histogram was calculated, and the laser Doppler imaging index was determined as the ratio of ischemic to nonischemic hindlimb blood perfusion. The normalized recovery index per animal was graphed and used for statistical analysis.

After the mice were euthanized, the vasculature was flushed with 0.9% normal saline containing heparin (1,000 IU/liter), papaverine (4 mg/liter), and adenosine (1 g/liter) for 3 min, as described before (Tirziu et al., 2005). For fixation, 2% paraformaldehyde was perfused for 5 min at 100 mm Hg pressure. 20% bismuth nanoparticles mixed in 5% gelatin were used as a microCT contrast agent and injected over 2 min with a syringe pump. The mice were then immediately chilled on ice and immersion-fixed in 2% paraformaldehyde overnight. The hindlimb vasculature was imaged with a high-resolution microCT imaging system (GE eXplore Locus SP), set to a 0.007-mm effective detector pixel size. Microview software (GE Healthcare) was used for initial reconstruction. Advanced workstation with various software was used for 3D reconstruction and segmentation. Quantification was performed by use of a National Institutes of Health Image. The data were expressed as vascular segment numbers, representing the total number of vessels, of specified diameter, counted in 200 z-sections for the thigh region and another 200 z-sections for the calf region.

RNAscope in situ hybridization

Aortic tissue segments were transferred into PCR tubes and subjected to RNAscope in a thermocycler with mouse anti-*Klf2*-C1 (510671; ACD) or mouse anti-*Nos3*-C1 (443061; ACD) labeled with Cy5 (FP1171; Perkin Elmer) and mouse *Cdh5*-C2 (132531; ACD) labeled with Cy3 (FP1170; Perkin Elmer) and DAPI. Aortas were then mounted on microscope slides en face. Endothelium, distal to intercostal branchpoints and displaying proper alignment, was imaged by widefield microscopy with a 60 \times oil objective. To quantify the *Klf2*-647 signal, background fluorescence was removed in ImageJ using a 1- μ m diameter rolling ball radius subtraction followed by despeckling (weighted average of a 3 \times 3-pixel grid). The resultant average fluorescence intensity of the field was divided by the number of ECs for three fields/mouse. Six mice were quantified for each group. For in vitro RNAscope labeling, MAEC were left static or subjected to 18 dynes/cm² laminar shear stress for 16 h before 30 min fixation in 3.7% formaldehyde. Slides were then labeled with *Klf2*-Cy5 according to the manufacturer's protocol and imaged using widefield microscopy.

Immunofluorescence

Cells were fixed with 3.7% formaldehyde for 10 min at room temp, permeabilized and blocked with 0.5× TBS startblock (37542; Thermo Fisher Scientific) + 0.3% Triton-X100 for 0.5–1 h room temp. Cells were then stained 4°C overnight in antibodies (See Table S6) diluted in 0.25× startblock + 0.1% Triton-X100. After 10 min washing in PBS, cells were subjected to 1–2 h staining in secondary antibody diluted in 0.25× startblock + 0.1% Triton-X100 before mounting in Fluoromount-G (Southern Biotech) and imaging. Widefield fluorescence microscopy was performed with a Nikon 80i equipped with 10× (NA 0.45), 20× (NA 0.75), and 60× (NA 1.40) objectives and a CCD camera (Retiga 200R; QImaging). Where indicated, spinning-disk confocal microscopy was performed with a Leica TCS SP8 inverted microscope using a 63× (NA 1.4) oil immersion objective.

Live cell imaging experiments were performed using chambers (1µm-Slide_I_0.4; Ibidi) perfused with a peristaltic pump (Masterflex C/L; Cole Parmer) and pressure dampener in an environmental chamber mounted upon a spinning disc confocal microscope (Leica sp8). For roGFP experiments, 3 × 3 or 5 × 5 fields were imaged within the middle of chambers with a 60× oil immersion objective. For mito-Keima experiments, confocal stacks were acquired using 20× air and 63× oil objectives with Ex/Em of both 405/590 and 552/590.

Image analysis

To quantify mitophagy using mito-Keima, 20× confocal stacks were flattened by Z-max projection and concatenated. Each channel of each image was uniformly auto-thresholded by the Moments method and the total mask area per channel per image was quantified. The mito-lysosomal fraction was calculated for each image (5–8 fields/condition) as $\text{Ex552}/(\text{Ex405} + \text{Ex552})$ and the mean taken from each condition per experiment.

To quantify Erk5 and p65 translocation in vitro and in vivo, images were collected from 3 to 4 aortas/group and were background-subtracted with a 40-µm rolling ball radius. 15-µm-wide line-scans were generated through the centers of endothelial cell nuclei (DAPI counterstained) to determine average pixel intensity at each position. The mean nuclear and cytoplasmic intensities were then recorded, and individual ratios (ERK5) or mean fluorescence units (p65) were determined.

Western blots were performed on 0.2-µm nitrocellulose membranes blocked with Starting Block (37542; Thermo Fisher Scientific). Images were quantified in ImageJ by performing traditional densitometry and normalization to actin or tubulin loading controls. Activation index quantification was performed by performing standard band densitometry on each band with a fixed ROI and quantifying the $([\text{ACTIVE}_{\text{MEAN}} - \text{BACKGROUND}_{\text{MEAN}}]/([\text{INACTIVE}_{\text{MEAN}} - \text{BACKGROUND}_{\text{MEAN}}] + [\text{ACTIVE}_{\text{MEAN}} - \text{BACKGROUND}_{\text{MEAN}}]))$. For MEKK3 activity quantification, distinct ROIs were often difficult to isolate. Therefore, lane-width line-scans were drawn through the center of the lane in ImageJ and the plot profile function was used to extract the peak intensity values of the upper and lower bands.

For quantification of colocalization, 63× confocal stacks were subjected to Z-max projection. Each channel was thresholded to

mask objects. Then Mander's Overlap Coefficient was calculated for the MEK5+/p62+ and p62+/Fis1^{TMD} regions.

Shear stress stimulation

Except for live imaging experiments, all shear stress experiments were performed in parallel plate flow chambers and perfused within a pump and environmental control system as described previously (Conway et al., 2017). Briefly, cells were seeded at 70–90% confluency on 10 µg/ml Fibronectin-coated glass slides for 48–72 h in complete medium. For shear stimulation, slides were mounted in custom-made 25 × 55-mm parallel plate shear chambers with 0.5-mm silicone gaskets and then stimulated with 18 dynes/cm² for LSS or 1 ± 3 dynes/cm² for OSS in complete media. The media was maintained at 37°C and 5% CO₂ with a heat gun and humidified bubbler, respectively.

IP

Antibodies used for co-IP are listed in Table S6. Resin was either GFP-trap (GTA-20; Chromotech) or ProteinA/G agarose (Santa Cruz), pre-bound with 2 µg antibody. Lysates were harvested in 25 mM Tris, pH 7.4, 100 mM NaCl, 1% TritonX-100, 0.2% sodium deoxycholate, 1.5× Complete EDTA-free Protease Inhibitor, and 1.5× PhosStop (Roche), clarified at 12,000 g 4°C, incubated with antibody-bound beads at 4°C overnight, and washed 3 times with 4°C lysis buffer. Bound protein was eluted with 2× protein sample buffer and subjected to SDS-PAGE.

Antibodies, vectors, dyes, and pharmacological reagents

Plasmids are listed in Table S3. sgRNA sequences are listed in Table S4. Antibodies are listed in Table S5. Drugs and dyes are listed in Table S6.

qPCR

To assay mitochondrial DNA content, mtDNA was prepped with genomic DNA columns and 50 ng subjected to qPCR with SybrGreen supermix in a BioRad CFX96 using 5'-CCCAGCTACTACCATCATTCAAGT-3' and 5'-GATGGTTTGGGAGATTGGTTGATGT-3', 28 cycles, 60°C annealing/extension, and denaturation curves (Rooney et al., 2015). Human and mouse *Klf2* qPCR were performed with primers listed in Table S7.

KO determination by Sanger sequencing

Genomic DNA was prepped and genomic loci about ±500 bp from the sgRNA landing areas were amplified and amplicons subjected to Sanger sequencing. The trace data were subjected to Synthego ICE analysis (Hsiau, 2019 Preprint).

Membrane fractionation

MAECs (approximately 3 × 10⁶ per condition) were incubated for 10 min in 10 mM Tris-HCl, pH 6.7, 10 mM KCl, 0.15 mM MgCl₂, 1 mM DTT, 1.5× Complete Protease inhibitor, and Phos-stop phosphatase inhibitor cocktails (Roche) on ice before homogenization by passing 20× through a 25-gauge needle. The homogenate was mixed with 2.5 M Sucrose to a 250-mM final concentration and centrifuged at 1,200 g for 10 min at 4°C. The resultant pellet was washed and labeled as the nuclear-enriched

fraction. The 1,200 g supernatant was centrifuged at 8,000 g for 10 min. The resultant pellet was washed and labeled as the mitochondrial-enriched fraction. The 8,000 g supernatant was further clarified at 21,000 g and then centrifuged again at 100,000 g for 90 min. The 100,000 g pellet was labeled as the small endomembrane-enriched fraction. The supernatant was precipitated with TCA and labeled as the cytosolic fraction.

Online supplemental material

Fig. S1 provides experimental details on the *Klf2*:GFP reporter and CRISPR screen's FACS sorting, library preparation, and quantification steps. **Fig. S2** describes characterization of the ERK5 MAPK pathway, gel-shifts, and nuclear translocation. **Fig. S3** provides supplemental evidence that p62 is involved in MEK5 signaling. **Fig. S4** shows a series of experiments testing the generalize role of autophagy, calcium, and mitochondrial function upon ERK5 and *Klf2*:GFP. **Fig. S5** details the role of PIEZO1 in regulating ERK5 signaling. Table S1 lists CRISPR screen loss-of-function hits and validation data. Table S2 summarizes data from the ERK5 activation mini-screen. Tables S3–S7 list the plasmids, sgRNAs, antibodies, drugs, and RT-PCR primers used in this study, respectively.

Acknowledgments

The authors thank Divyesh Joshi (Yale University) for scientific discussion and critical reading of the manuscript; Brielle Hayward and Elizabeth Min (Yale University) for assistance with shear stress experiments; Geoffrey Lyon and Ann Haberman (Yale University) for FACS assistance; Kaya Bilguvar and Chris Castaldi (Yale University) for library prep and sequencing advice; Anna-Maija Penttinen (Université de Montréal, Montréal, Quebec, Canada) for preparing material from PINK1 KO mice; Andres Hidalgo (Yale University), Arul Jayaraman (Texas A&M University), and Patty Lee (Yale University) for reagents; and Cristina Cavinato and Jay Humphrey (Yale University) for additional mouse experimentation. We also thank Carlo Millia (Vesalius Research Center, Leuven, Belgium) for initial studies on REDOX and laminar shear stress.

This work was supported by the American Heart Association grants AHA #13POST16720007 and AHA #17SDG33400173 to B.G. Coon; by National Institutes of Health grant R01 HL75092 and a Leducq Trans-Atlantic Network Grant to M.A. Schwartz; by the European Research Council Consolidator Grant-Rendox (ERC-CoG 647057) and Associazione Italiana Ricerca sul Cancro Investigator Grant 20119 to M. Santoro; and by the Krembil and Brain Canada foundations and the Canadian Institutes of Health Research to L.-E. Trudeau.

The authors declare no competing financial interests.

Author contributions: B.G. Coon and M.A. Schwartz: conceptualization, project administration, formal analysis, supervision, funding acquisition, and writing. B.G. Coon: investigation, methodology, data curation. B.G. Coon, M. Astone, S. Timalsina, and J. Themen: data curation, investigation, and validation. Z. Zhang: methodology and formal analysis. J. Fang and J. Han: methodology. M. Chung: investigation and validation. Y.J. Yang-Klingler, M. Jain, K.K.

Hirschi, and L.-E. Trudeau: resources. M. Santoro: resources, investigation, and formal analysis.

Submitted: 28 September 2021

Revised: 15 March 2022

Accepted: 11 May 2022

References

- Abe, J.-i., and B.C. Berk. 2014. Novel mechanisms of endothelial mechanotransduction. *Arterioscler. Thromb. Vasc. Biol.* 34:2378–2386. <https://doi.org/10.1161/ATVBAHA.114.303428>
- Abe, J., M. Kusuohara, R.J. Ulevitch, B.C. Berk, and J.D. Lee. 1996. Big mitogen-activated protein kinase 1 (BMK1) is a redox-sensitive kinase. *J. Biol. Chem.* 271:16586–16590. <https://doi.org/10.1074/jbc.271.28.16586>
- Ahmed, S.M.U., L. Luo, A. Namani, X.J. Wang, and X. Tang. 2017. Nrf2 signaling pathway: Pivotal roles in inflammation. *Biochim. Biophys. Acta (BBA) - Mol. Basis Dis.* 1863:585–597. <https://doi.org/10.1016/j.bbadis.2016.11.005>
- Akundi, R.S., Z. Huang, J. Eason, J.D. Pandya, L. Zhi, W.A. Cass, P.G. Sullivan, and H. Bueler. 2011. Increased mitochondrial calcium sensitivity and abnormal expression of innate immunity genes precede dopaminergic defects in Pink1-deficient mice. *PLoS One.* 6:e16038. <https://doi.org/10.1371/journal.pone.0016038>
- Allen, G.F.G., R. Toth, J. James, and I.G. Ganley. 2013. Loss of iron triggers PINK1/Parkin-independent mitophagy. *EMBO Rep.* 14:1127–1135. <https://doi.org/10.1038/embor.2013.168>
- Birdsey, G.M., A.V. Shah, N. Dufton, L.E. Reynolds, L. Osuna Almagro, Y. Yang, I.M. Aspalter, S.T. Khan, J.C. Mason, E. Dejana, et al. 2015. The endothelial transcription factor ERG promotes vascular stability and growth through Wnt/ β -catenin signaling. *Dev. Cell.* 32:82–96. <https://doi.org/10.1016/j.devcel.2014.11.016>
- Caradu, C., T. Couffinhal, C. Chapouly, S. Guimbal, P.L. Hollier, E. Ducasse, A. Bura-Riviere, M. Dubois, A.P. Gadeau, and M.A. Renault. 2018. Restoring endothelial function by targeting desert hedgehog downstream of Klf2 improves critical limb ischemia in adults. *Circ. Res.* 123:1053–1065. <https://doi.org/10.1161/CIRCRESAHA.118.313177>
- Chappell, D.C., S.E. Varner, R.M. Nerem, R.M. Medford, and R.W. Alexander. 1998. Oscillatory shear stress stimulates adhesion molecule expression in cultured human endothelium. *Circ. Res.* 82:532–539. <https://doi.org/10.1161/01.res.82.5.532>
- Chatterjee, S., and A.B. Fisher. 2014. Mechanotransduction in the endothelium: Role of membrane proteins and reactive oxygen species in sensing, transduction, and transmission of the signal with altered blood flow. *Antioxid. Redox Signal.* 20:899–913. <https://doi.org/10.1089/ars.2013.5624>
- Ciffa, R., T. Lemark, A.K. Tarafder, A. Guesdon, S. Rybina, W.J.H. Hagen, T. Johansen, and C. Sachse. 2015. The selective autophagy receptor p62 forms a flexible filamentous helical scaffold. *Cell Rep.* 11:748–758. <https://doi.org/10.1016/j.celrep.2015.03.062>
- Conway, D.E., B.G. Coon, M. Budatha, P.T. Arsenovic, F. Orsenigo, F. Wessel, J. Zhang, Z. Zhuang, E. Dejana, D. Westweber, and M.A. Schwartz. 2017. VE-cadherin phosphorylation regulates endothelial fluid shear stress responses through the polarity protein LGN. *Curr. Biol.* 27:2727. <https://doi.org/10.1016/j.cub.2017.08.064>
- Das, H., A. Kumar, Z. Lin, W.D. Patino, P.M. Hwang, M.W. Feinberg, P.K. Majumder, and M.K. Jain. 2006. Kruppel-like factor 2 (KLF2) regulates proinflammatory activation of monocytes. *Proc. Natl. Acad. Sci. USA.* 103:6653–6658. <https://doi.org/10.1073/pnas.0508235103>
- Dekker, R.J., S. van Soest, R.D. Fontijn, S. Salamanca, P.G. de Groot, E. Van Bavel, H. Pannekoek, and A.J.G. Horrevoets. 2002. Prolonged fluid shear stress induces a distinct set of endothelial cell genes, most specifically lung Kruppel-like factor (KLF2). *Blood.* 100:1689–1698. <https://doi.org/10.1182/blood-2002-01-0046>
- Duchemin, A.L., H. Vignes, and J. Vermot. 2019. Mechanically activated piezo channels modulate outflow tract valve development through the Yap1 and Klf2-Notch signaling axis. *Elife.* 8:e44706. <https://doi.org/10.7554/eLife.44706>
- Erazo, T., A. Moreno, G. Ruiz-Babot, A. Rodriguez-Asiain, N.A. Morrice, J. Espadamala, J.R. Bayascas, N. Gomez, and J.M. Lizcano. 2013. Canonical and kinase activity-independent mechanisms for extracellular signal-regulated kinase 5 (ERK5) nuclear translocation require dissociation of

- Hsp90 from the ERK5-Cdc37 complex. *Mol. Cell Biol.* 33:1671–1686. <https://doi.org/10.1128/MCB.01246-12>
- Faber, J.E., W.M. Chilian, E. Deindl, N. van Royen, and M. Simons. 2014. A brief etymology of the collateral circulation. *Arterioscler. Thromb. Vasc. Biol.* 34:1854–1859. <https://doi.org/10.1161/ATVBAHA.114.303929>
- Fang, J.S., B.G. Coon, N. Gillis, Z. Chen, J. Qiu, T.W. Chittenden, J.M. Burt, M.A. Schwartz, and K.K. Hirschi. 2017. Shear-induced Notch-Cx37-p27 axis arrests endothelial cell cycle to enable arterial specification. *Nat. Commun.* 8:2149. <https://doi.org/10.1038/s41467-017-01742-7>
- Geisler, S., K.M. Holmstrom, D. Skujat, F.C. Fiesel, O.C. Rothfuss, P.J. Kahle, and W. Springer. 2010. PINK1/Parkin-mediated mitophagy is dependent on VDAC1 and p62/SQSTM1. *Nat. Commun.* 12:119–131. <https://doi.org/10.1038/ncb2012>
- Gherardi, G., H. Monticelli, R. Rizzuto, and C. Mammucari. 2020. The mitochondrial Ca²⁺ uptake and the fine-tuning of aerobic metabolism. *Front. Physiol.* 11:554904. <https://doi.org/10.3389/fphys.2020.554904>
- Hahn, C., and M.A. Schwartz. 2009. Mechanotransduction in vascular physiology and atherogenesis. *Nat. Rev. Mol. Cell Biol.* 10:53–62. <https://doi.org/10.1038/nrm2596>
- Heil, M., and W. Schaper. 2004. Influence of mechanical, cellular, and molecular factors on collateral artery growth (arteriogenesis). *Circ. Res.* 95:449–458. <https://doi.org/10.1161/01.RES.0000141145.78900.44>
- Hsiao, T., D. Conant, N. Rossi, T. Maures, K. Waite, J. Yang, S. Joshi, R. Kelso, K. Holden, B.L. Enzmann, and R. Stoner. 2019. Inference of CRISPR Edits from sanger trace data. *bioRxiv*. <https://doi.org/10.1101/251082> (Preprint posted August 10, 2019.)
- Isogai, S., D. Morimoto, K. Arita, S. Unzai, T. Tenno, J. Hasegawa, Y.S. Sou, M. Komatsu, K. Tanaka, M. Shirakawa, and H. Tochio. 2011. Crystal structure of the ubiquitin-associated (UBA) domain of p62 and its interaction with ubiquitin. *J. Biol. Chem.* 286:31864–31874. <https://doi.org/10.1074/jbc.M111.259630>
- Jain, A., T. Lamark, E. Sjøttem, K.B. Larsen, J.A. Awuh, A. Overvatn, M. McMahon, J.D. Hayes, and T. Johansen. 2010. p62/SQSTM1 is a target gene for transcription factor NRF2 and creates a positive feedback loop by inducing antioxidant response element-driven gene transcription. *J. Biol. Chem.* 285:22576–22591. <https://doi.org/10.1074/jbc.M110.118976>
- Jain, M.K., P. Sangwung, and A. Hamik. 2014. Regulation of an inflammatory disease: Kruppel-like factors and atherosclerosis. *Arterioscler. Thromb. Vasc. Biol.* 34:499–508. <https://doi.org/10.1161/ATVBAHA.113.301925>
- Kant, S., K.-V. Tran, M. Kvandova, A.D. Caliz, H.J. Yoo, H. Learnard, A.C. Dolan, S.M. Craige, J.D. Hall, J.M. Jimenez, et al. 2022. PGC1 alpha regulates the endothelial response to fluid shear stress via telomerase reverse transcriptase control of heme oxygenase-1. *Arterioscler. Thromb. Vasc. Biol.* 42:19–34. <https://doi.org/10.1161/ATVBAHA.121.317066>
- Krause, M.D., R.T. Huang, D. Wu, T.P. Shentu, D.L. Harrison, M.B. Whalen, L.K. Stolze, A. Di Rienzo, I.P. Moskowitz, M. Civelek, et al. 2018. Genetic variant at coronary artery disease and ischemic stroke locus 1p32.2 regulates endothelial responses to hemodynamics. *Proc. Natl. Acad. Sci. USA.* 115:E11349–E11358. <https://doi.org/10.1073/pnas.1810568115>
- Kumar, A., Z. Lin, S. SenBanerjee, and M.K. Jain. 2005. Tumor necrosis factor alpha-mediated reduction of KLF2 is due to inhibition of MEF2 by NF-kappaB and histone deacetylases. *Mol. Cell Biol.* 25:5893–5903. <https://doi.org/10.1128/MCB.25.14.5893-5903.2005>
- Lamark, T., M. Perander, H. Outzen, K. Kristiansen, A. Overvatn, E. Michaelsen, G. Bjorkoy, and T. Johansen. 2003. Interaction codes within the family of mammalian Phox and Bem1p domain-containing proteins. *J. Biol. Chem.* 278:34568–34581. <https://doi.org/10.1074/jbc.M303221200>
- Lee, H.Y., S.W. Youn, H.J. Cho, Y.W. Kwon, S.W. Lee, S.J. Kim, Y.B. Park, B.H. Oh, and H.S. Kim. 2013. FOXO1 impairs whereas statin protects endothelial function in diabetes through reciprocal regulation of Kruppel-like factor 2. *Cardiovasc. Res.* 97:143–152. <https://doi.org/10.1093/cvr/cvs283>
- Lee, J.S., Q. Yu, J.T. Shin, E. Sebзда, C. Bertozzi, M. Chen, P. Mericko, M. Stadtfeld, D. Zhou, L. Cheng, et al. 2006. Klf2 is an essential regulator of vascular hemodynamic forces in vivo. *Dev. Cell.* 11:845–857. <https://doi.org/10.1016/j.devcel.2006.09.006>
- Lewis, S.C., L.F. Uchiyama, and J. Nunnari. 2016. ER-mitochondria contacts couple mtDNA synthesis with mitochondrial division in human cells. *Science.* 353:aaf5549. <https://doi.org/10.1126/science.aaf5549>
- Li, J., B. Hou, S. Tumova, K. Muraki, A. Bruns, M.J. Ludlow, A. Sedo, A.J. Hyman, L. McKeown, R.S. Young, et al. 2014. Piezo1 integration of vascular architecture with physiological force. *Nature.* 515:279–282. <https://doi.org/10.1038/nature13701>
- Liang, X., T. Zhang, L. Shi, C. Kang, J. Wan, Y. Zhou, J. Zhu, and M. Mi. 2015. Ampelopsin protects endothelial cells from hyperglycemia-induced oxidative damage by inducing autophagy via the AMPK signaling pathway. *Biofactors.* 41:463–475. <https://doi.org/10.1002/biof.1248>
- Liu, Y., H. Zhao, H. Li, B. Kalyanaraman, A.C. Nicolosi, and D.D. Gutterman. 2003. Mitochondrial sources of H2O2 generation play a key role in flow-mediated dilation in human coronary resistance arteries. *Circ. Res.* 93:573–580. <https://doi.org/10.1161/01.RES.0000091261.19387.AE>
- Long, J., T.P. Garner, M.J. Pandya, C.J. Craven, P. Chen, B. Shaw, M.P. Williamson, R. Layfield, and M.S. Searle. 2010. Dimerisation of the UBA domain of p62 inhibits ubiquitin binding and regulates NF-kappaB signalling. *J. Mol. Biol.* 396:178–194. <https://doi.org/10.1016/j.jmb.2009.11.032>
- Moscat, J., M.T. Diaz-Meco, A. Albert, and S. Campuzano. 2006. Cell signaling and function organized by PB1 domain interactions. *Mol. Cell.* 23:631–640. <https://doi.org/10.1016/j.molcel.2006.08.002>
- Murohara, T., T. Asahara, M. Silver, C. Bauters, H. Masuda, C. Kalka, M. Kearney, D. Chen, J.F. Symes, M.C. Fishman, et al. 1998. Nitric oxide synthase modulates angiogenesis in response to tissue ischemia. *J. Clin. Invest.* 101:2567–2578. <https://doi.org/10.1172/JCI1560>
- Nakamura, K., and G.L. Johnson. 2003. PB1 domains of MEKK2 and MEKK3 interact with the MEK5 PB1 domain for activation of the ERK5 pathway. *J. Biol. Chem.* 278:36989–36992. <https://doi.org/10.1074/jbc.C300313200>
- Nakamura, K., A.J. Kimple, D.P. Siderovski, and G.L. Johnson. 2010. PB1 domain interaction of p62/sequestosome 1 and MEKK3 regulates NF-kappaB activation. *J. Biol. Chem.* 285:2077–2089. <https://doi.org/10.1074/jbc.M109.065102>
- Ni, C.W., S. Kumar, C.J. Ankeny, and H. Jo. 2014. Development of immortalized mouse aortic endothelial cell lines. *Vasc. Cell.* 6:7. <https://doi.org/10.1186/2045-824X-6-7>
- Parmar, K.M., H.B. Larman, G. Dai, Y. Zhang, E.T. Wang, S.N. Moorthy, J.R. Kratz, Z. Lin, M.K. Jain, M.A. Gimbrone Jr., and G. Garcia-Cardena. 2006. Integration of flow-dependent endothelial phenotypes by Kruppel-like factor 2. *J. Clin. Invest.* 116:49–58. <https://doi.org/10.1172/JCI24787>
- Princely Abudu, Y., S. Pankiv, B.J. Mathai, A. Hakon Lystad, C. Bindesboll, H.B. Brenne, M. Yoke Wui Ng, B. Thiede, A. Yamamoto, T. Mutugi Nthiga, et al. 2019. NIPSNAP1 and NIPSNAP2 act as “Eat Me” signals for mitophagy. *Dev. Cell.* 49:509–525.e12. <https://doi.org/10.1016/j.devcel.2019.03.013>
- Ranade, S.S., Z. Qiu, S.H. Woo, S.S. Hur, S.E. Murthy, S.M. Cahalan, J. Xu, J. Mathur, M. Bandell, B. Coste, et al. 2014. Piezo1, a mechanically activated ion channel, is required for vascular development in mice. *Proc. Natl. Acad. Sci. USA.* 111:10347–10352. <https://doi.org/10.1073/pnas.1409233111>
- Rooney, J.P., I.T. Ryde, L.H. Sanders, E.H. Howlett, M.D. Colton, K.E. Gern, G.D. Mayer, J.T. Greenamyre, and J.N. Meyer. 2015. PCR based determination of mitochondrial DNA copy number in multiple species. *Methods Mol. Biol.* 1241:23–38. https://doi.org/10.1007/978-1-4939-1875-1_3
- Sanchez-Martin, P., and M. Komatsu. 2018. p62/SQSTM1: Steering the cell through health and disease. *J. Cell Sci.* 131:jcs222836. <https://doi.org/10.1242/jcs.222836>
- Santo-Domingo, J., L. Vay, E. Hernandez-Sanmiguel, C.D. Lobaton, A. Moreno, M. Montero, and J. Alvarez. 2007. The plasma membrane Na⁺/Ca²⁺ exchange inhibitor KB-R7943 is also a potent inhibitor of the mitochondrial Ca²⁺ uniporter. *Br. J. Pharmacol.* 151:647–654. <https://doi.org/10.1038/sj.bjp.0707260>
- Scheitlin, C.G., J.A. Julian, S. Shanmughapriya, M. Madesh, N.M. Tsoukias, and B.R. Alevriadou. 2016. Endothelial mitochondria regulate the intracellular Ca²⁺ response to fluid shear stress. *Am. J. Physiol. Cell Physiol.* 310:C479–C490. <https://doi.org/10.1152/ajpcell.00171.2015>
- Shalem, O., N.E. Sanjana, E. Hartenian, X. Shi, D.A. Scott, T.S. Mikkelsen, D. Heckl, B.L. Ebert, D.E. Root, J.G. Doench, and F. Zhang. 2014. Genome-scale CRISPR-Cas9 knockout screening in human cells. *Science.* 343:84–87. <https://doi.org/10.1126/science.1247005>
- Shirihai, O.S., M. Song, and G.W. Dorn 2nd. 2015. How mitochondrial dynamism orchestrates mitophagy. *Circ. Res.* 116:1835–1849. <https://doi.org/10.1161/CIRCRESAHA.116.306374>
- Sohn, S.J., D. Li, L.K. Lee, and A. Winoto. 2005. Transcriptional regulation of tissue-specific genes by the ERK5 mitogen-activated protein kinase. *Cell. Mol. Biol.* 25:8553–8566. <https://doi.org/10.1128/MCB.25.19.8553-8566.2005>
- Tirziu, D., K.L. Moodie, Z.W. Zhuang, K. Singer, A. Helisch, J.F. Dunn, W. Li, J. Singh, and M. Simons. 2005. Delayed arteriogenesis in hypercholesterolemic mice. *Circulation.* 112(16):2501–2509. <https://doi.org/10.1161/CIRCULATIONAHA.105.542829>

- Vion, A.C., M. Kheloufi, A. Hammoutene, J. Poisson, J. Lasselin, C. Devue, I. Pic, N. Dupont, J. Busse, K. Stark, et al. 2017. Autophagy is required for endothelial cell alignment and atheroprotection under physiological blood flow. *Proc. Natl. Acad. Sci. USA*. 114:E8675–E8684. <https://doi.org/10.1073/pnas.1702223114>
- Wang, S., R. Chennupati, H. Kaur, A. Iring, N. Wettschureck, and S. Offermanns. 2016. Endothelial cation channel PIEZO1 controls blood pressure by mediating flow-induced ATP release. *J. Clin. Invest.* 126:4527–4536. <https://doi.org/10.1172/JCI87343>
- Wang, X., X. Fang, J. Zhou, Z. Chen, B. Zhao, L. Xiao, A. Liu, Y.S.J. Li, J.Y.J. Shyy, Y. Guan, et al. 2013. Shear stress activation of nuclear receptor PXR in endothelial detoxification. *Proc. Natl. Acad. Sci. USA*. 110:13174–13179. <https://doi.org/10.1073/pnas.1312065110>
- Weikel, K.A., J.M. Cacicedo, N.B. Ruderman, and Y. Ido. 2015. Glucose and palmitate uncouple AMPK from autophagy in human aortic endothelial cells. *Am. J. Physiol. Cell Physiol.* 308:C249–C263. <https://doi.org/10.1152/ajpcell.00265.2014>
- Yamamoto, K., Y. Nogimori, H. Imamura, and J. Ando. 2020. Shear stress activates mitochondrial oxidative phosphorylation by reducing plasma membrane cholesterol in vascular endothelial cells. *Proc. Natl. Acad. Sci. USA*. 117:33660–33667. <https://doi.org/10.1073/pnas.2014029117>
- Yoshii, S.R., and N. Mizushima. 2017. Monitoring and measuring autophagy. *Int. J. Mol. Sci.* 18:E1865. <https://doi.org/10.3390/ijms18091865>
- Young, A., W. Wu, W. Sun, H. Benjamin Larman, N. Wang, Y.S. Li, J.Y. Shyy, S. Chien, G. Garcia-Cardena, and G. Garcia-Cardena. 2009. Flow activation of AMP-activated protein kinase in vascular endothelium leads to Kruppel-like factor 2 expression. *Arterioscler. Thromb. Vasc. Biol.* 29:1902–1908. <https://doi.org/10.1161/ATVBAHA.109.193540>
- Yu, J., E.D. deMuinck, Z. Zhuang, M. Drinane, K. Kauser, G.M. Rubanyi, H.S. Qian, T. Murata, B. Escalante, and W.C. Sessa. 2005. Endothelial nitric oxide synthase is critical for ischemic remodeling, mural cell recruitment, and blood flow reserve. *Proc. Natl. Acad. Sci. USA*. 102:10999–11004. <https://doi.org/10.1073/pnas.0501444102>
- Zakkar, M., K. Van der Heiden, L.A. Luong, H. Chaudhury, S. Cuhlmann, S.S. Hamdulay, R. Krams, I. Edirisinghe, I. Rahman, H. Carlsen, et al. 2009. Activation of Nrf2 in endothelial cells protects arteries from exhibiting a proinflammatory state. *Arterioscler. Thromb. Vasc. Biol.* 29:1851–1857. <https://doi.org/10.1161/ATVBAHA.109.193375>
- Zhang, Y., M. Sauler, A.S. Shinn, H. Gong, M. Haslip, P. Shan, P. Mannam, and P.J. Lee. 2014. Endothelial PINK1 mediates the protective effects of NLRP3 deficiency during lethal oxidant injury. *J. Immunol.* 192:5296–5304. <https://doi.org/10.4049/jimmunol.1400653>
- Zhao, X., T. Duong, C.C. Huang, S.R. Kain, and X. Li. 1999. Comparison of enhanced green fluorescent protein and its destabilized form as transcription reporters. *Methods Enzymol.* 302:32–38. [https://doi.org/10.1016/s0076-6879\(99\)02006-6](https://doi.org/10.1016/s0076-6879(99)02006-6)
- Zhong, F., H. Chen, C. Wei, W. Zhang, Z. Li, M.K. Jain, P.Y. Chuang, H. Chen, Y. Wang, S.K. Mallipattu, and J.C. He. 2015. Reduced Kruppel-like factor 2 expression may aggravate the endothelial injury of diabetic nephropathy. *Kidney Int.* 87:382–395. <https://doi.org/10.1038/ki.2014.286>
- Zhuang, Z.W., J. Shi, J.M. Rhodes, M.J. Tsapakos, and M. Simons. 2011. Challenging the surgical rodent hindlimb ischemia model with the miniinterventional technique. *J. Vasc. Interv. Radiol.* 22(10):1437–1446. <https://doi.org/10.1016/j.jvir.2010.12.039>

Supplemental material

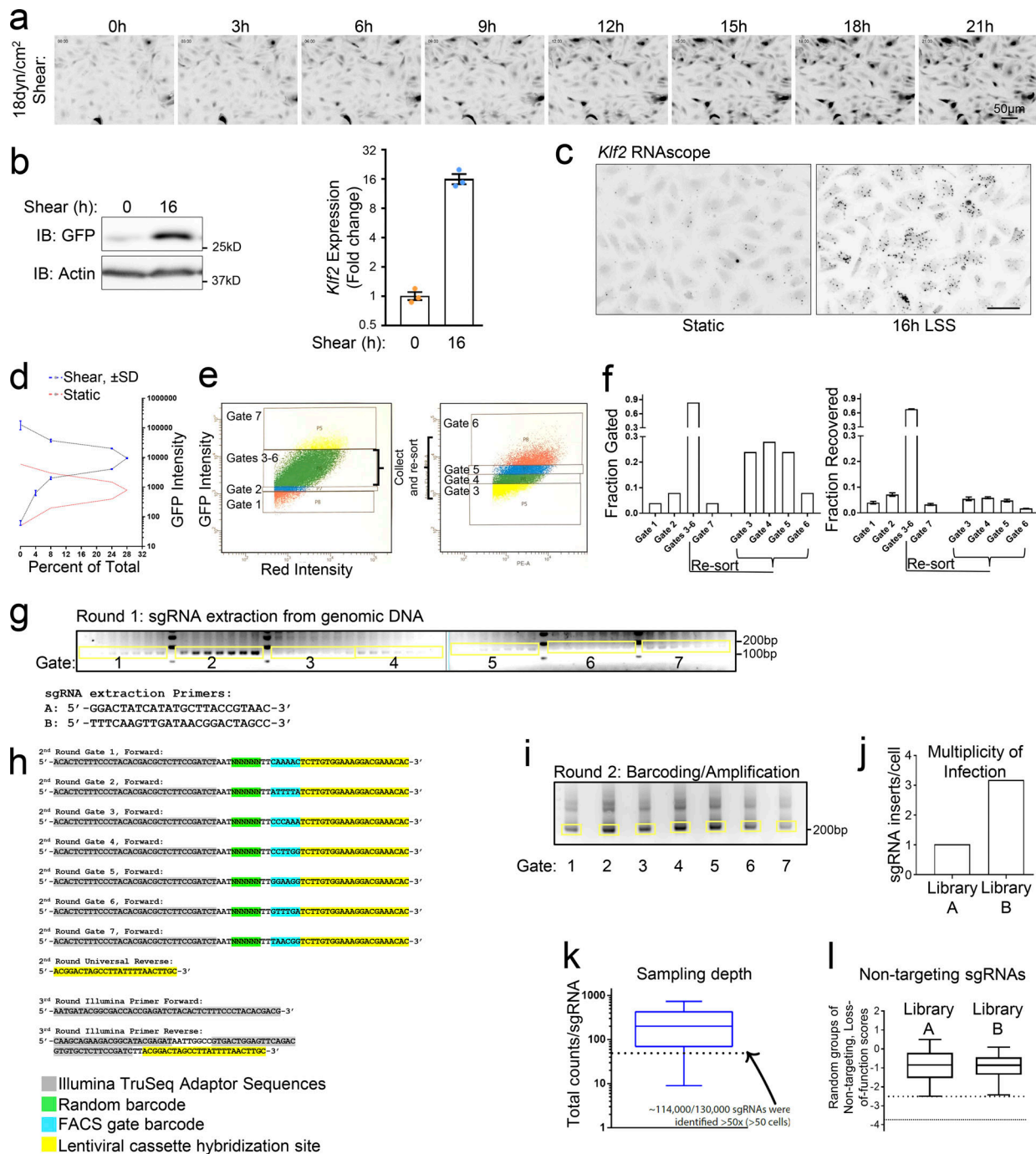


Figure S1. **CRISPR screening and production of sequencing libraries.** (a) Time-lapse images for EGFP in MAEC *Klf2*:d2EGFP reporter cells stimulated with 18 dynes/cm² LSS. Images presented in inverted grayscale for enhanced contrast. *n* = 2. (b) Induction of MAEC *Klf2*:d2EGFP reporter cells compared to endogenous *KLF2* in MAECs stimulated with LSS, assayed by qPCR. *n* = 3. (c) Endogenous *Klf2* induction by LSS in MAECs assayed by RNAscope. Images are presented in inverted grayscale for enhanced contrast. *n* = 2. Scale = 50 μ m. (d) *Klf2* reporter cells' fluorescence intensity distribution across seven FACS gate boundaries was graphed from three replicate experiments to reveal reproducibility. Dashed lines are means of *n* = 3, and blue error bars represent SD. (e) Strategy utilized to isolate the seven gates described in Fig. 1 c. (f) Quantification of the total gated and recovered fractions of FACS-sorted cells. (g) Lentiviral cassettes were extracted from genomic DNA and resolved by agarose gel electrophoresis. (h) Adaptors used for second and third round amplification of sgRNA cassettes. Round 2 amplification used a nested PCR strategy that labels the sgRNA with a random barcode and FACS gate ID barcode. Round 3 PCR attaches the sample barcode and the TruSeq adaptor sequences. (i) Barcoded sgRNAs were resolved by agarose electrophoresis following round 2 labeling/amplification. Excised bands used for Illumina sequencing are labeled in yellow. (j) After sequencing and removing replicate reads, the library complexity was divided by the number of sorted cells to confirm that each half of the lentiviral library (A/B) was transduced with a low MOI. (k) The unique copy number of each of the 130,000 sgRNAs was plotted as a 1–99% box and whisker graph. sgRNAs that are represented <50 \times , which comprise ~12% of the total, were excluded from further analysis. (l) Of the 1,000 nontargeting sgRNAs in each library, the three lowest scoring from random groups of six were summed and plotted. These resultant loss-of-function scores can be compared to Fig. 1 e. The lower first and fifth percentile boundaries are marked by dashed lines. Source data are available for this figure: SourceData F51.

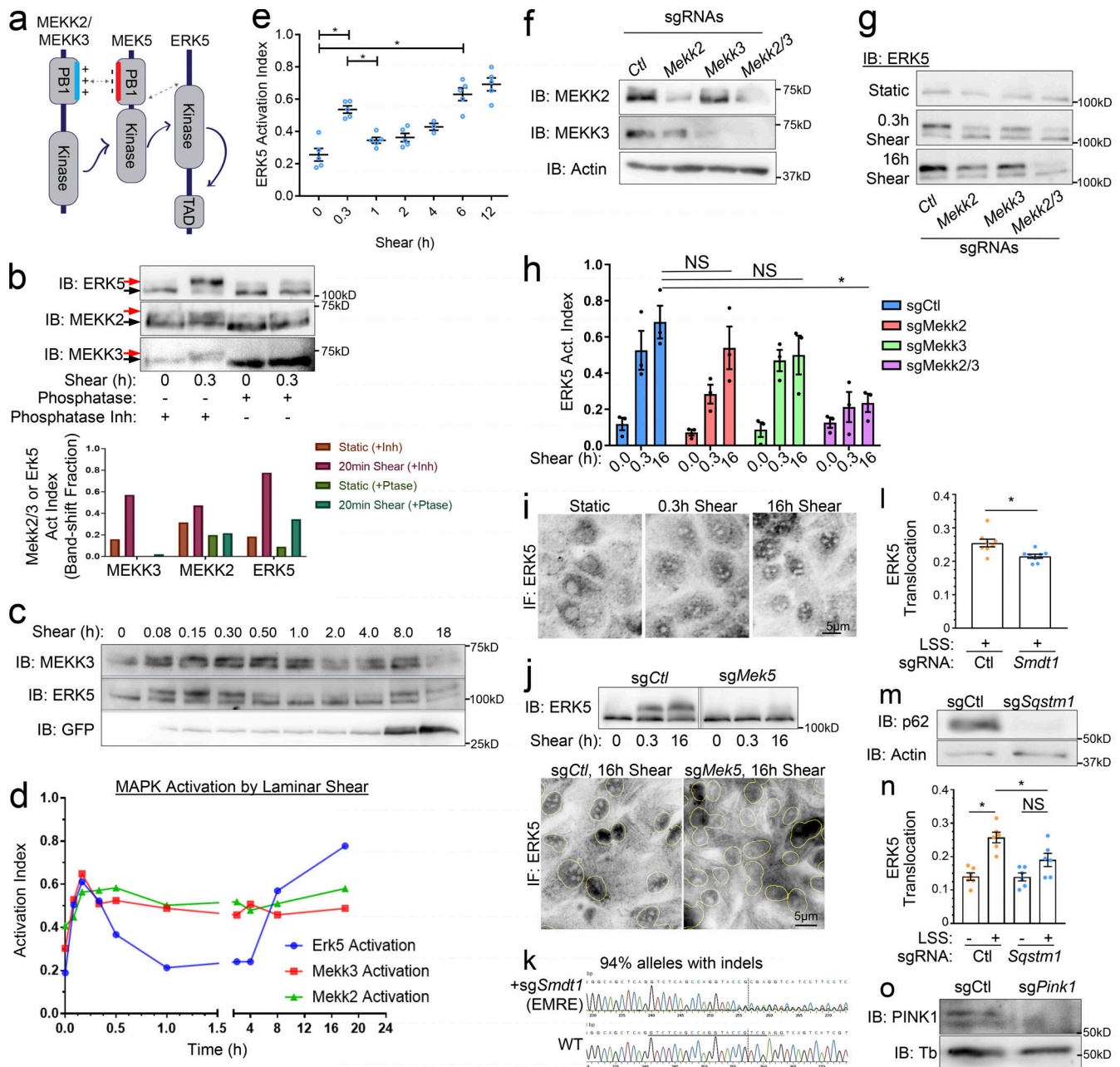


Figure S2. The MAPK cascade regulating *Klf2* induction. (a) Domain architecture and interactions in the MEK2/3–MEK5–ERK5 complex. MEK2/3 and MEK5 PB1 domains’ basic and acidic patches dimerize to promote signaling. (b) Representative shear-induced gel-shifts for MEK2, MEK3, and ERK5. The lower and gel-shifted upper bands are indicated with black and red arrows, respectively. (b) Lysates from MAECs with or without 18 dynes/cm² shear for 0.3 h were treated with alkaline phosphatase or phosphatase inhibitor as indicated. Gel shifts were quantified by densitometry. *n* = 3. (c) Time course of MEK3 and ERK5 activation and *Klf2* reporter induction in shear-stimulated MAECs. (d) Quantification of MEK2, MEK3, and ERK5 activation in shear-stimulated MAECs at various times by gel shift assay. Data are representative of *n* = 3. (e) Reproducibility of shear-stimulated ERK5 activation dynamics determined by gel shift assays. *n* = 5. (f) Validation of MEK2 and MEK3 KO. (g and h) Representative blots and quantification of ERK5 activation from control, MEK2, and/or MEK3 KOs stimulated with LSS for the indicated times. *n* = 3. (i) ERK5 staining showing nuclear translocation after shear. (j) Shear-induced ERK5 activation and nuclear translocation in MAECs after MEK5 KO. (k) Sanger sequencing and Indel analysis of genomic DNA to assess sg-*Smdt1* indels (EMRE-KO efficiency). Data were analyzed with the Synthego ICE toolbox. (l) Quantification of nuclear ERK5 in shear-stimulated Ctl- and EMRE-KOs. Translocation = nuclear/total signal. (m) Validation of p62-KO with anti-*Sqstm1* sgRNAs by Western blot. (n) Quantification of nuclear ERK5 in shear-stimulated Ctl- and p62-KOs. (o) Validation of PINK1-KO by Western blot. *, *P* < 0.05 by one-way ANOVA (e and h), Student’s *t* test (l), or two-way ANOVA (n). Source data are available for this figure: SourceData F52.

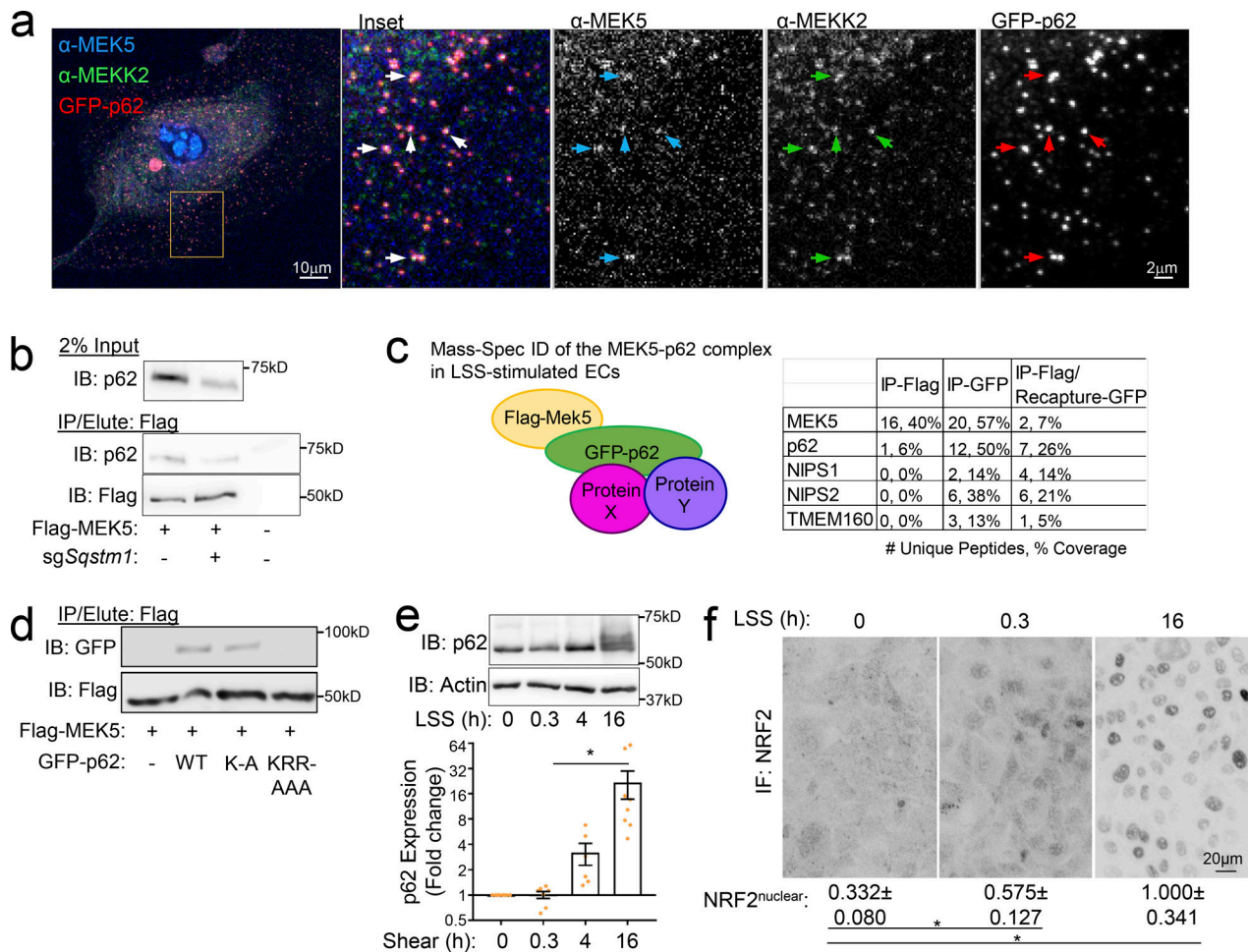


Figure S3. p62 assembles a p62-MAPK complex. (a) HUVECs were transduced with GFP-p62 lentivirus, subjected to LSS for 3 h, fixed, and stained for endogenous MEKK2 and MEK5. Arrows: three-channel colocalization in dense p62 + punctae. (b) HUVECs with or without p62 knockdown and expressing MEK5-Flag were subjected to anti-Flag immunoprecipitation and Flag peptide elution. Eluted proteins were subjected to anti-Flag and anti-p62 immunoblotting. (c) Schematic for isolation of MEK5-p62 complex by dual IP. HUVECs expressing MEK5-Flag and GFP-p62 were subjected to LSS for 3 h then IPed with anti-FLAG or anti-GFP resin. One half of the Flag IP was eluted with Flag peptide and IPed with anti-GFP. The resultant MEK5-p62 complex was analyzed by mass spectrometry to identify and quantify interaction partners. The number of unique peptides and percent protein coverage from each group are shown. (d) HUVECs expressing MEK5-Flag and WT or mutant GFP-p62 constructs were IPed with anti-Flag, eluted with Flag peptide, and analyzed by immunoblotting. (e) MAECs were exposed to LSS for the indicated times and lysates immunoblotted for p62 and actin as a loading control. Graph: quantified p62 levels from individual independent experiments. Values are means ± SEM. (f) MAECs stimulated with LSS for the indicated times were fixed, stained for NRF2, and nuclear intensity quantified. Images are inverted to enhance contrast. Data are representative of three independent experiments. *, P < 0.05 by one-way ANOVA. Source data are available for this figure: SourceData FS3.

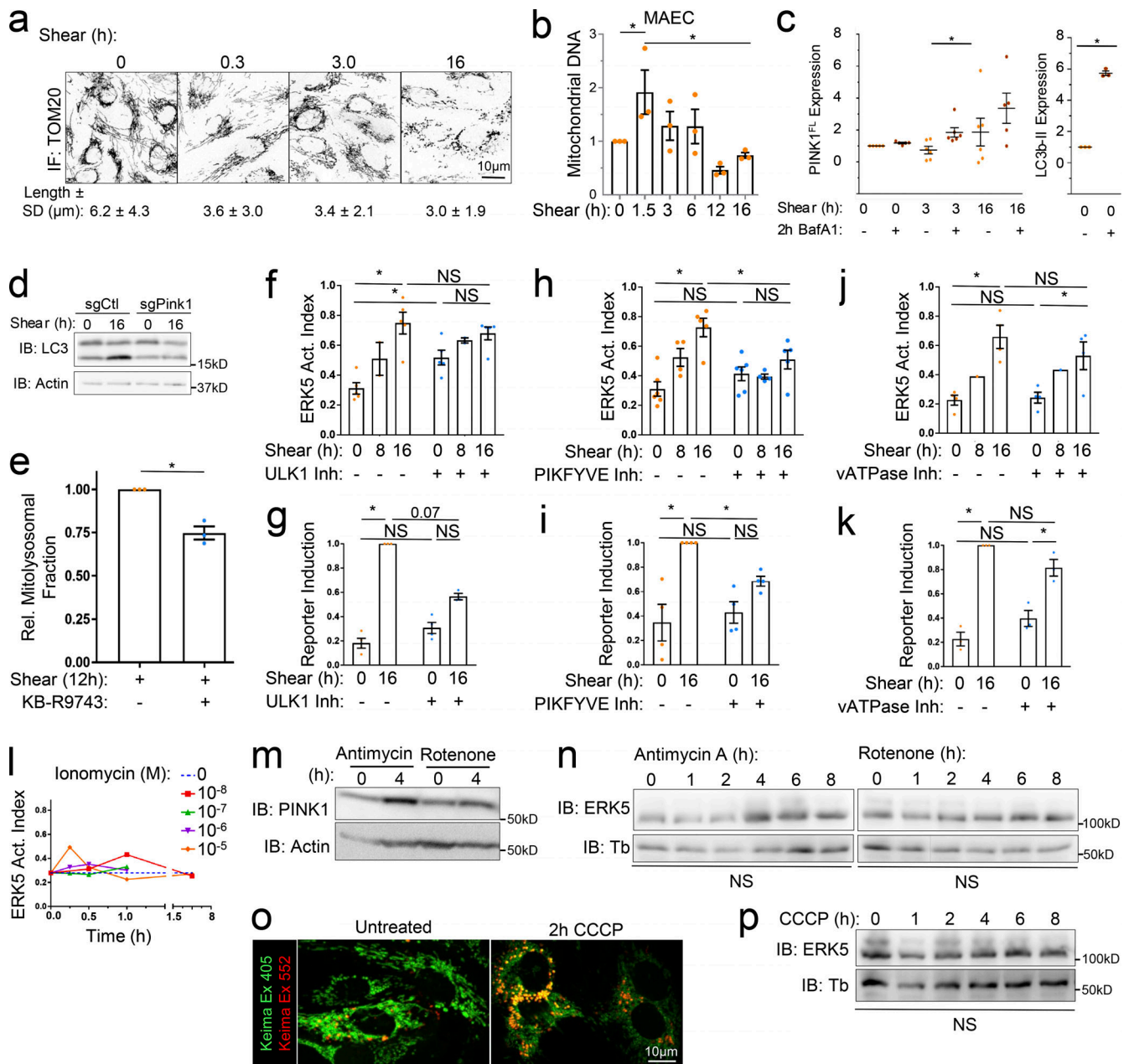


Figure S4. Role of autophagy and mitochondria in regulating the ERK5 pathway. (a) HUVECs were subjected to 18 dynes/cm² LSS for the indicated times, stained for TOMM20, imaged using confocal microscopy at 63× magnification, and mitochondrial length quantified. Values are means ± SD; N = 110–200 cells. (b) MAEC mitochondrial DNA content was assayed by qPCR at the indicated times. (c) To assay mitophagic flux, MAECs were subjected to LSS for the indicated times ± BafA1 for the final 2 h. Lysates were then immunoblotted for full length PINK1 (~62 kD) and actin as a loading control. BafA1-dependent accumulation serves as a metric for mitophagy. LC3b-II accumulation is shown as a positive control for BafA1 treatment. (d) LC3b-II accumulation after PINK1-KO, representative of three experiments. (e) HUVECs expressing mito-Keima were subjected to 12 h LSS with or without KB-R9743. The mito-lysosomal fraction was then quantified as in Fig. 2 i. n = 3. (f–k) MAECs treated with inhibitors of ULK1 (MRT68921, 1 μM), PIKFYVE (YM201636, 200 nM), or vATPase (BafA1, 100 nM) were exposed to LSS for the indicated times, then lysates analyzed for ERK5 activation or *Klf2* reporter induction. (l) MAECs were stimulated with Ionomycin for the indicated times and concentrations, and ERK5 activation assayed. n = 3. (m) HUVECs treated with Antimycin-A (2 μM) or Rotenone (100 nM) for the indicated times were assayed for PINK1 levels. n = 3. (n) HUVECs treated with Antimycin-A or Rotenone were assayed for ERK5 activation. n = 3. (o) Mito-Keima-transduced HUVECs were treated with 10 μM carbonyl cyanide m-chlorophenyl hydrazone (CCCP) for 2 h and subjected to confocal microscopy. n = 3. (p) Cells treated with CCCP for the indicated times were assayed for ERK5 activation. n = 3. *, P < 0.05 by one-way ANOVA (b, n, and p), Student's t test (e), or two-way ANOVA (f–k). Source data are available for this figure: SourceData FS4.

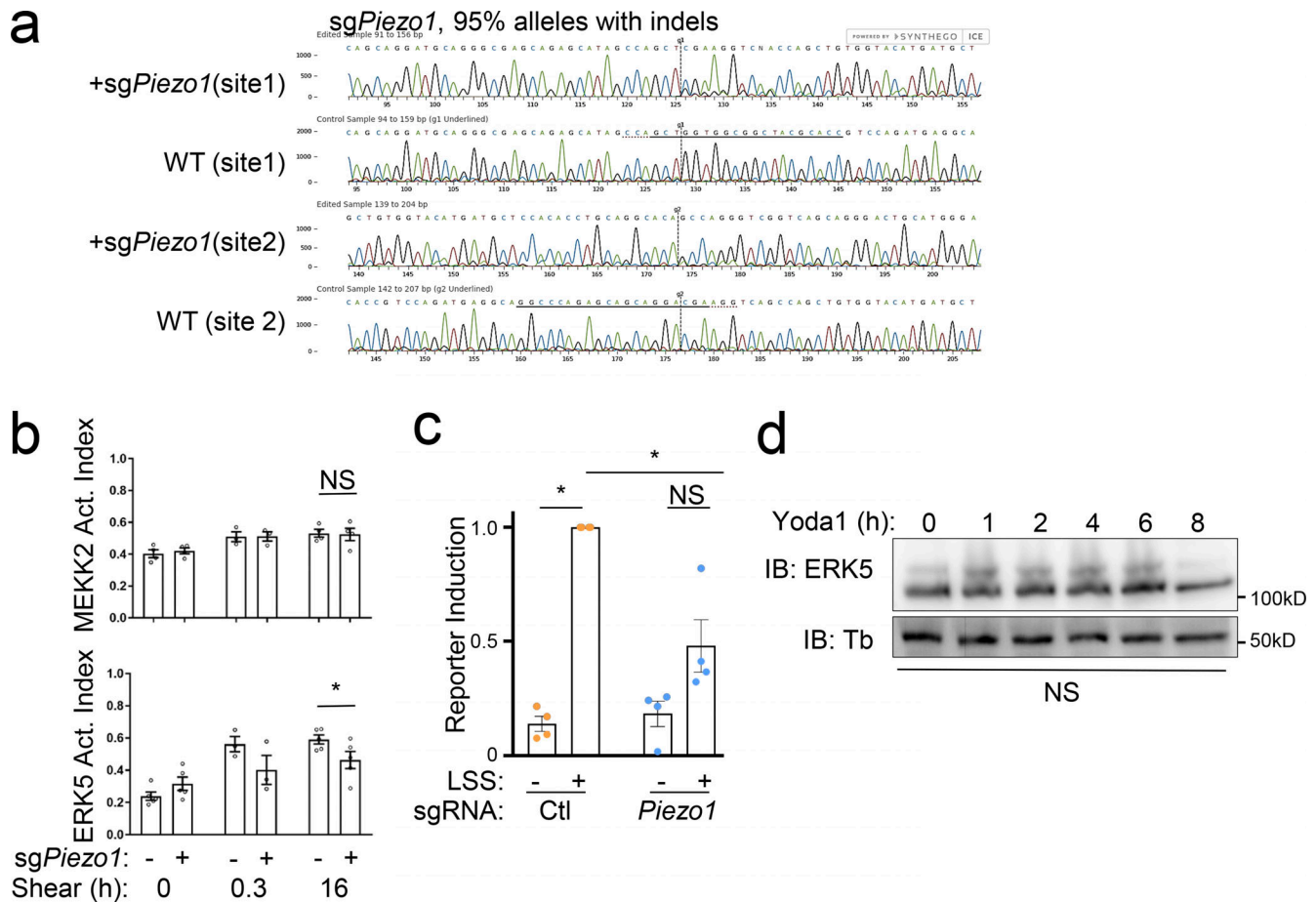


Figure S5. **PIEZO1 and the *Klf2* pathway.** (a) CRISPR KO of PIEZO1 demonstrated by Sanger sequencing of genomic DNA. Analysis using the Synthego ICE toolbox reveals 95% of the alleles have indels. (b) MEKK2 and ERK5 activation after PIEZO1-KO quantified from gel shift assay. Values are means \pm SEM, $n = 3-5$. (c) Quantification of *Klf2*:GFP induction after 16 h LSS, in control and PIEZO1-KO. Values are means \pm SEM; $n = 3$. (d) MAECs treated with 1 μ M Yoda1, a PIEZO1 agonist, for the indicated times, were analyzed by immunoblotting for ERK5 activation and *Klf2*:GFP induction. $n = 3$. *, $P < 0.05$ by Student's t test or one-way ANOVA (b and c). Source data are available for this figure: SourceData F55.

Provided online are seven tables. Table S1 lists CRISPR screen hits. Table S2 lists early-onset ERK5 regulator screen. Table S3 lists plasmid DNAs. Table S4 lists unique sgRNA sequences. Table S5 lists antibody usage. Table S6 lists drugs. Table S7 lists PCR primers.